UNIVERSITY *of the* WESTERN CAPE

FACULTY OF NATURAL SCIENCES

DEPARTMENT OF PHYSICS AND ASTRONOMY

$E2/M1$ mixing in the $J^{\pi} = 5/2^{+}$ to $3/2^{+}$ transition in ^{21}Na and its relation to the ^{20}Ne(p, γ) stellar reaction rate

Supervisor:

SMARAJIT TRIAMBAK

Candidate:

SUMEERA GOPAL

A thesis submitted in fulfillment of the requirements for the degree of Master of Sciences in Physics

Declaration

I, Sumeera Gopal, hereby declare the work presented in this thesis entitled **"$E2/M1$ mixing in the $J^\pi = 5/2^+$ to $3/2^+$ transition in ^{21}Na and its relation to the ^{20}Ne(p,γ) stellar reaction rate"** is my own work. This thesis has not been submitted to any other institutions or university for examination. All materials and sources used through out this thesis has been made references to.
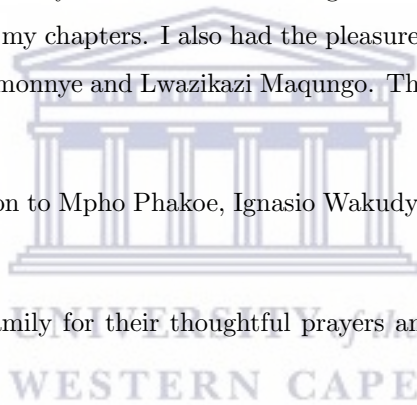
Signed:

Date: 02/02/2023

Acknowledgements

I am grateful to my supervisor Prof Smarajit Triambak for giving me the opportunity to work on this project. His guidance and endless assistance on this project is greatly appreciated.

A sincere thank you to Bhivek Singh for his advice and assistance during my data analysis. I am grateful for your mentorship during my MSc. journey. Thanks should also go to Mohammed Kamil and Craig Vyfers for assisting me with the write-up of my chapters. I also had the pleasure of working with Jespere Nzobadila Ondze, Odwa Tyuka, Goistseona Ramonnye and Lwazikazi Maqungo. Thank you all for your encouragement and support.

I would like to extend my appreciation to Mpho Phakoe, Ignasio Wakudyanaye, Bako Audu and Joy Nyondo for their amazing friendship.

Finally, I would like to thank my family for their thoughtful prayers and tremendous love throughout my studies. God bless!

Contents

iv

List of Figures

List of Tables

Preamble

Measurements of nuclear reaction rates are important to understand the nucleosynthesis of elements in stars. However, direct measurements of such reaction rates are difficult because of low cross sections at stellar temperatures.

This thesis focuses on the $^{20}\text{Ne}(p,\gamma)^{21}\text{Na}$ bottleneck reaction that is part of the neon-sodium (NeNa) cycle and plays a critical role in the creation of Ne, Na and Mg isotopes [1]. The $^{20}\text{Ne}(p,\gamma)$ reaction is important in the hydrogen-burning shells of red giants, cores of massive stars, Asymptotic Giant Branch (AGB) stars and cataclysmic variables called nova explosions [2, 3]. For determining the reaction rate, one requires an accurate knowledge of both non-resonant and resonant contributions. In the latter category, a critical resonance produces the $J^{\pi} = 5/2^{+}$, $E_{\text{x}} = 3544.3$ keV state in ^{21}Na [1]. As the dominant decay mode of this level is via a γ-ray transition to the $3/2^{+}$ ground state in ^{21}Na, measuring the $E2/M1$ (electric quadrupole to magnetic dipole) mixing ratio of this transition forms an important aspect of the reaction rate measurement. This thesis describes a measurement of this mixing ratio, whose value was last published nearly six decades ago [4].

The thesis is made up of five chapters:

- The first chapter briefly describes stellar evolution and nucleosynthesis. Following this, the neon-sodium cycle and the importance of the $^{20}\text{Ne}(p,\gamma)^{21}\text{Na}$ reaction is motivated so that it lays the foundation for the following chapters.

- In the second chapter I provide a theoretical background on both the nuclear and astrophysics aspects of this study. Technical aspects of nuclear reactions and the essential measurements pertinent to this work are discussed.

- The third chapter briefly provides experimental details of the mixing ratio measurement for the 3544.3 keV $\rightarrow$ ground state (G.S.) transition in ^{21}Na.

- The fourth chapter presents the data analysis and results.

- The last chapter provides brief concluding remarks.

1

Chapter 1

Introduction

1.1 The nuclear physics of stars

The cycle of a star begins when large molecular gas clouds collapse due to their gravitational energy being greater than the thermal energy of the molecules in the cloud. In such a scenario,

$$\frac{GM^2}{R} \geq \frac{3}{2} kT \frac{M}{m}.$$
(1.1)

This condition of instability is called the Jeans criterion. Equation 1.1 is rewritten as [5]

$$M \geq 3.7 \left(\frac{kT}{Gm} \right)^{3/2} \rho^{-1/2}.$$
(1.2)

In the above, M is the total mass of the molecular cloud, R is its radius, k is Boltzmann's constant, G is the gravitational constant, T is the cloud temperature, m is the mean molecular weight, and ρ is the cloud molecular density. Interstellar clouds typically have densities of about 100 atoms cm^{-3} and $T \simeq 100$ K. The Jeans criterion is only met when the mass of the cloud is greater than 2×10^4 $M_\odot$ [5] (where $M_\odot$ denotes one solar mass).

The genesis of stars is initiated through such condensation of gas clouds in interstellar space. The gravitational collapse to a high central density results in the formation of a protostar. The internal heat that is generated is radiated away from the center, which is relatively hotter than the surface. The protostar's core is prevented from further collapse due to hydrostatic equilibrium, whereby the internal pressure from the

2

core counterbalances gravitational contraction. The internal outward pressure is due to the thermal energy of the gas within the star and due to the outward flow of radiation. The latter is significant in massive stars. The temperature of a star determines the type of electromagnetic radiation that it gives out. For example in the case of protostars, the emission of infrared radiation has been observed [6]. When these photons interact with any opaque material they exert a radiation pressure

$$p = \frac{4\sigma}{3c}T^4, \tag{1.3}$$

where σ is the Stefan-Boltzmann constant and c is the speed of light. In the absence of radiation pressure, such as in the case of white dwarfs with masses $< 1.44 \ M_\odot$ (the Chandrasekhar limit), electron degeneracy pressure aids in preventing gravitational collapse. This is because Pauli's exclusion principle prevents electrons with the same quantum numbers from occupying the same energy state within a stellar plasma. For a star in hydrostatic equilibrium, the pressure gradient is

$$\frac{dP(r)}{dr} = \frac{-GM(r)\rho(r)}{r^2}, \tag{1.4}$$

where $P(r)$ and $\rho(r)$ are the total gas pressure and the density at a radial distance r, respectively. Here, $M(r)$ is the mass of gas inside a stellar sphere of radius r, so that

$$M(r) = \int_0^r 4\pi r^2 \rho(r) dr. \tag{1.5}$$

If one assumes that $M(r) = \frac{M}{2}$ at $r = \frac{R}{2}$, where M and R are the mass and radius of the star, then it is easy to show that the density at the midway point is [5]

$$\bar{\rho} \simeq M/R^3. \tag{1.6}$$

If the pressure on the surface at $r = R$ is such that $P(R) \to 0$, then the central pressure $P(0)$ can be estimated to be [5]

$$P(0) \simeq \frac{8\rho_s GM}{R}, \tag{1.7}$$

where ρ_s is the mean density of the star.

The equation of state relates the pressure, temperature and density of matter in a stellar interior. Using the ideal gas equation it is easy to show that

3

$$P(r) = \frac{k\rho(r)T(r)}{m},\tag{1.8}$$

where k is the Boltzmann's constant and m denotes the mean molecular weight of the gas particles, $m \simeq 1/2m_H$. Using the above equation, and further assuming that the central density $\rho(0) = 2\rho$, the central temperature of the star is approximated to be

$$T(0) \simeq \frac{mGM}{kR}.\tag{1.9}$$

Once a protostar is stabilized by hydrostatic equilibrium, it reaches the main-sequence stage [7] in the Hertzsprung-Russell (HR) diagram shown in Fig. 1.1. As energy is radiated away, the star begins to shrink due to gravitational compression. This compression increases the heat within the interior of the star. When the temperature of the core reaches approximately 10^7 K, the thermonuclear fusion of hydrogen nuclei is initiated [5]. During the course of hydrogen burning, gravitational contraction is halted and the star maintains a nearly constant size, temperature and luminosity. The rate at which hydrogen is converted into helium mainly depends on the mass of the star. Large-mass stars are known to burn hydrogen much faster compared to low-mass stars.

Main sequence stars, shown in the HR diagram (Fig. 1.1), predominantly have hydrogen available for fuel and energy is generated within their cores via the proton-proton (pp) chain reaction, which is shown in Fig. 1.2.

In the first step of the pp chain, two protons fuse to form a deuteron via the weak interaction process

$$p + p \rightarrow {}^{2}_{1}\text{D} + e^{+} + \nu_e.\tag{1.10}$$

The Q value of this reaction is $Q = 1.442$ MeV, which is released and shared among the reaction products [10].

The deuteron produced in this first step fuses with another proton producing ^{3}He through the process

$$ {}^{2}_{1}\text{D} + p \rightarrow {}^{3}_{2}\text{He} + \gamma.\tag{1.11}$$

4
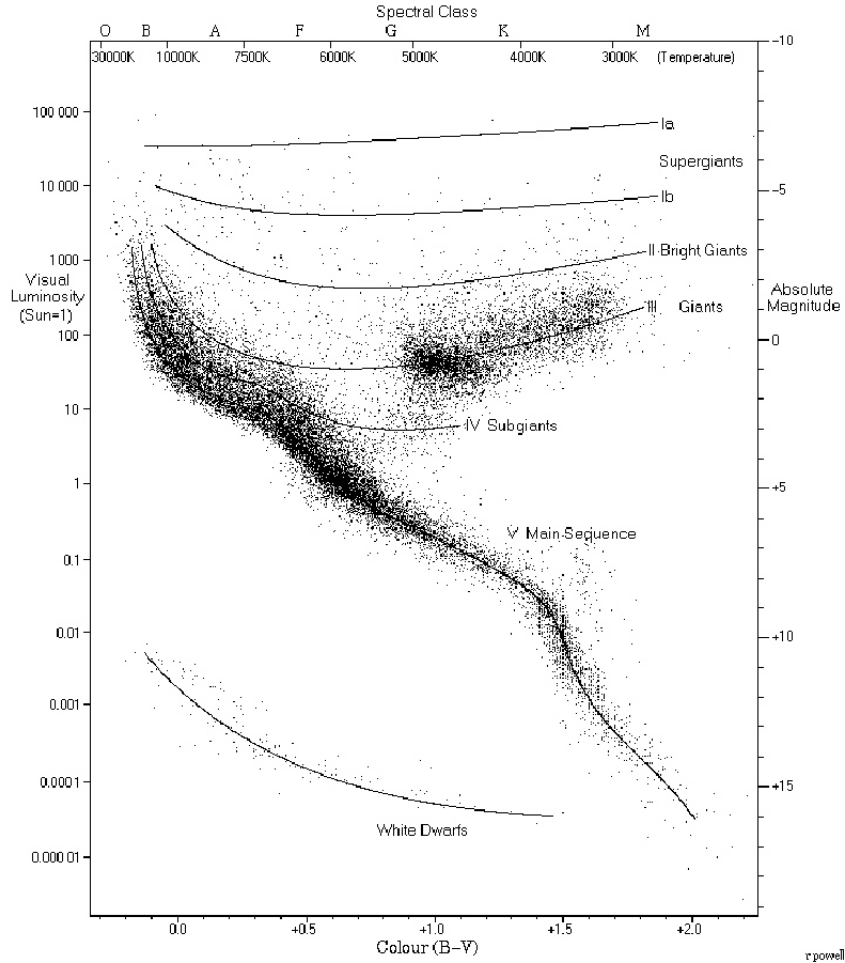
Figure 1.1: The Hertzsprung-Russell (HR) diagram classifies stars. The left y-axis shows the luminosity relative to the sun, whereas the right y-axis displays the absolute magnitude in comparison with the sun. The upper x-axis shows the temperature and spectral type, while the color index is shown on the lower x-axis. This figure is taken from Ref. [8].

Following this, a series of reactions leads to the formation of heavier elements. As shown in Fig 1.2, two ^{3}He nuclei fuse to yield α particles through the ^{3}He$(^3$He$, 2p)\alpha$ reaction. This is followed by reactions such as ^{3}He$(\alpha, \gamma)^7$Be, ^{7}Be$(p, \gamma)^8$B, ^{8}B β^+ decay, ^{7}Be β^- decay, ^{7}Li$(p, \alpha)\alpha$, etc. [5,10]. Clearly, the pp reaction is the most fundamental for energy generation in stars. This reaction is extremely slow as it is mediated by the weak interaction. Without this reaction none of the heavier elements would form.

A star will continue to be in the main-sequence region until the hydrogen fuel in its core is exhausted. Then gravitational contraction will take over again, causing the star to compress further. The core at this stage

5
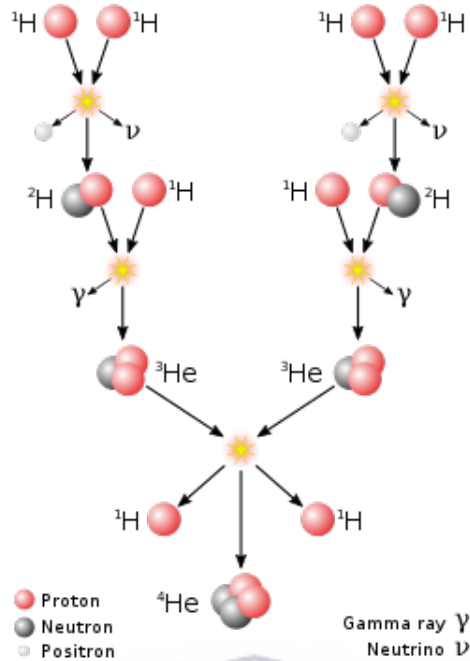
Figure 1.2: The proton-proton chain. Figure taken from Ref. [9].

mainly consists of helium whereas the shell surrounding the helium core is hydrogen. Energy generated within the core due to this compression is usually more than can be radiated away at the surface. Therefore the outer layers of the core expand and cool. At this stage the star becomes brighter and appears to be redder, forming a red giant, which is located along the line of giants in the HR diagram in Fig. 1.1. At this point the central temperature of the star is high enough to ignite helium burning. Stars similar to our sun will burn helium as soon the hydrogen fuel is consumed [5, 10–12]. A critical reaction here is the triple-alpha process, $3\alpha \rightarrow {}^{12}C$, due to a resonance (the Hoyle state) at 7.65 MeV in ${}^{12}C$.

An important group of stars in the HR diagram lies towards the left of the red giants, called asymptotic giant branch (AGB) stars [10]. In massive stars with $M \geq 8M_\odot$ the ashes of one set of nuclear reactions become fuel for the next set. The helium burning produces elements such as carbon and oxygen, with a small amount of neon. At even higher temperatures carbon and oxygen undergo reactions via the CNO cycle, which will be described below. This cycle initiates a series of nucleosynthesis processes that lead to the creation of heavier elements. At higher temperatures, elements up to Fe are produced. This is shown schematically in Fig. 1.3, as a typical onion shell structure of a star.

The CNO cycle also plays a major role in the energy production in the stars. It has two sub-parts to it, as shown in Fig. 1.4. Depending on a star's interior, at low temperatures ($T \sim 20$ MK) the CN cycle is

6
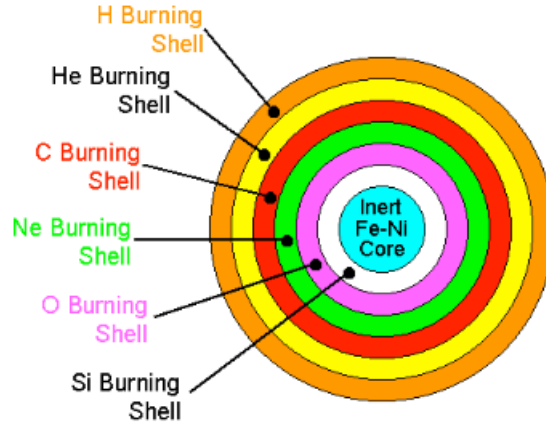
Figure 1.3: The layered onion ring structure of a supergiant star.

dominant, whereas the NO cycle proceeds at much higher temperatures ($T \gtrsim 30$ MK) [13].

As shown in Figs. 1.4 and 1.5, the CN cycle proceeds via

$$^{12}\text{C}(p,\gamma)^{13}\text{N}(\beta^+\nu)^{13}\text{C}(p,\gamma)^{14}\text{N}(p,\gamma)^{15}\text{O}(\beta^+\nu)^{15}\text{N}(p,\alpha)^{12}\text{C},$$
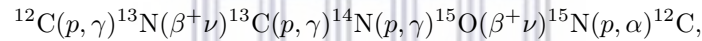
whereas the second part, the NO cycle goes as

$$^{16}\text{O}(p,\gamma)^{17}\text{F}(\beta^+,\nu)^{17}\text{O}(p,\alpha)^{14}\text{N}(p,\gamma)^{15}\text{O}(\beta^+,\nu)^{15}\text{N}(p,\gamma)^{16}\text{O}.$$
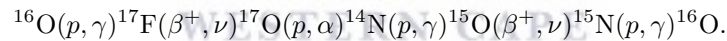
The CNO cycle is catalytic, as it reuses carbon, nitrogen and oxygen both as starting and end products. It also produces helium through (p,α) reactions. The reactions for proton capture and β decay compete with each other. At higher temperatures proton captures dominate β decays, therefore the cycle is referred to as the hot CNO cycle. At lower temperatures the time scales for energy production are dominated by the β decay half lives. This is referred to the cold CNO cycle.

Once the core reaches the pure iron stage, further nucleosynthesis ceases. This is because (as shown in Fig. 1.6) Fe has a large binding energy per nucleon. This prevents further nuclear reactions and energy production to counterbalance gravitational collapse. Therefore the core will continue to shrink and this causes the star to become unstable. In many cases, for masses $\geq 8 M_\odot$ [5], stars shed their mass via a violent explosion known as a Type 2 supernova. The remnant of a Type 2 supernova is a highly dense core, which

7
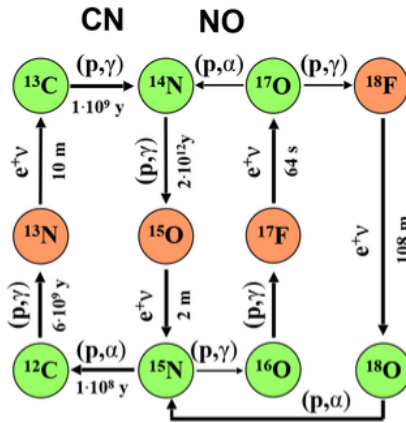
Figure 1.4: The CNO cycle.
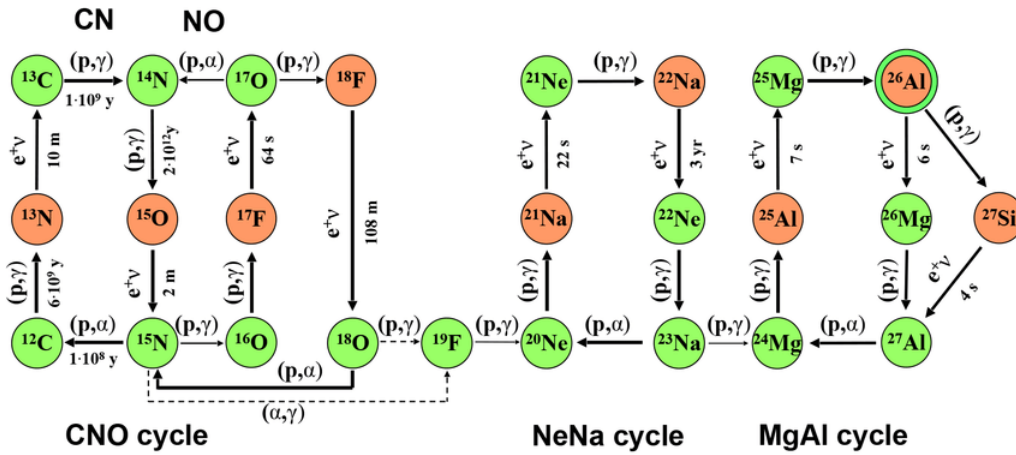
Figure 1.5: The CNO, NeNa and MgAl Cycles.

may take the form of a neutron star or a black hole.

Stars with masses $M \leq 8M_\odot$ result in the formation of a planetary nebula, leaving behind a white dwarf. Other stars in binary systems (shown in Fig. 1.7) tend to shed their mass via the nova phenomenon or as Type 1 supernovae. These are similar short-lived cataclysmic phenomena.

In binary systems comprising white dwarfs, as the normal star has exhausted its hydrogen fuel within the core, the shell (consisting of mostly hydrogen) expands outwards and cools, becoming a red giant. During this expansion matter crosses over the Roche surface, as shown in Fig. 1.7. The expelled material that is swept in to the vicinity of the accretion disk spirals into the white dwarf at extreme velocities. This leads to a thermonuclear runaway, resulting in the occurrence of a series of nuclear reactions. Since reactions involving hydrogen occur more easily, cycles such as the CNO (and NeNa and MgAl cycles described below) are possible [16–20]. A Type 1 supernova can also occur in such binary systems. This is much more violent

8
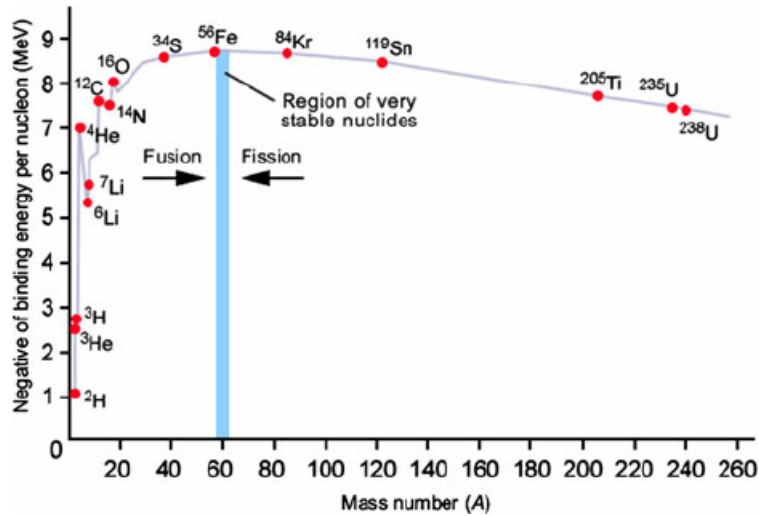
Figure 1.6: Binding energy per nucleon as a function of the mass number A. Taken from Ref. [14].
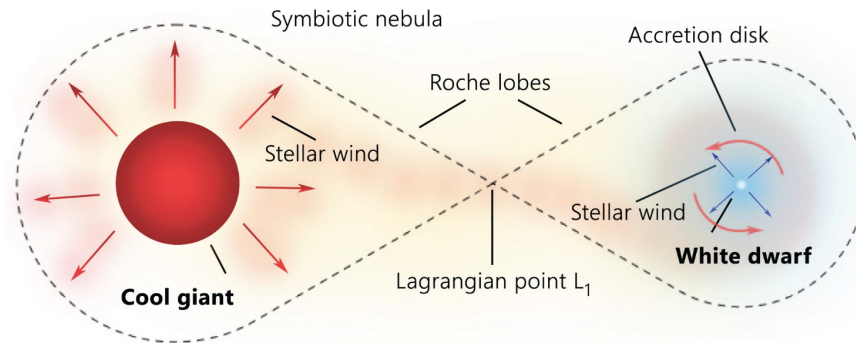
Figure 1.7: Schematic representation of a binary stellar system. Figure taken from Ref. [15].

and results in the destruction of the whole star instead of just its hydrogen envelope.

As shown in Fig. 1.5, the CNO cycle results in the formation of ^{18}O, which leads to ^{15}N via the ^{18}O(p, α) reaction. Break out from the CNO cycle to the NeNa cycle occurs via the ^{15}N(α, γ), ^{18}O(p, γ) and ^{19}F(p, γ) reactions. The ^{23}Na(p, γ) reaction is an important reaction, linking the NeNa and the MgAl cycles.

The pp chain and the CNO cycle contribute mostly to the energy production in stars, whereas the NeNa and MgAl cycles are vital for the production of new elements between ^{20}Ne and ^{27}Al.

At the extreme temperatures that occur in environments such as classic novae, the breakout reactions mentioned above become important. We focus next on the NeNa cycle, which is important in the context of this project.

9

1.2   The Neon-Sodium Cycle

The nucleosynthesis of Ne, Na and Mg isotopes is largely influenced by the important ^{20}Ne$(p, \gamma)^{21}$Na reaction. As Fig. 1.5 shows, these isotopes are produced through a series of proton captures and β decays that begin with ^{20}Ne. The ^{20}Ne$(p, \gamma)^{21}$Na reaction is important in stellar environments where temperatures are greater than 0.05 GK, such as in the hydrogen-burning shells of red giants, cores of massive stars, AGB stars and novae [2,3]. It also results in the production of ^{22}Na, an important isotope for observational astronomy [3,21]. Furthermore, the ^{20}Ne$(p, \gamma)^{21}$Na reaction rate is one of the slowest, which makes it an important regulatory point in the cycle [21].

Although there are several ^{20}Ne$(p, \gamma)^{21}$Na resonances that contribute to the stellar reaction rate (see Fig 1.8), a few important points are worth considering. The reaction Q value is 2431.6 keV. It is known from previous work [22] that at low temperatures the reaction rate proceeds mainly via non-resonant capture and the tail of the sub-threshold resonance at 2424.9 keV. At higher temperatures ($T \approx 1$ GK) the main contribution to the reaction rate is from the resonant capture on the 3544.3 keV state, whose spin-parity is $J^{\pi} = \frac{5}{2}^{+}$ (this state is highlighted in Fig 1.8). Aspects concerning this resonance state are discussed further in the following chapters.
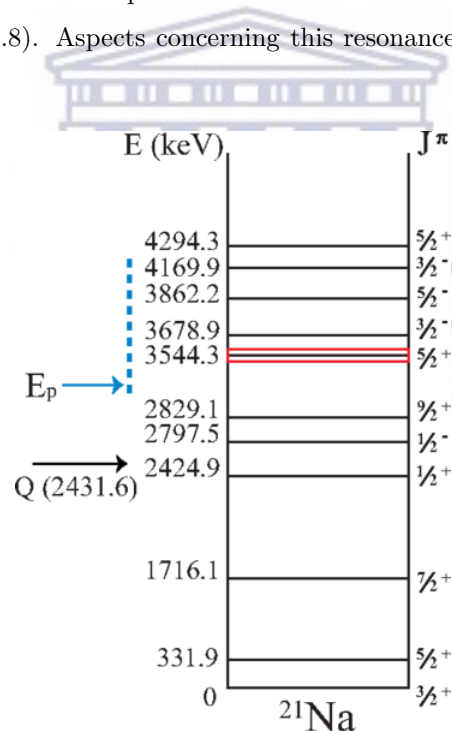
Figure 1.8: Energy level diagram for ^{21}Na, taken from Ref. [1].

Chapter 2

The ^{20}Ne$(p, \gamma)^{21}$Na reaction: Nuclear physics background

2.1 Concepts

Here I first introduce some background concepts, before discussing both general and special aspects of the ^{20}Ne(p, γ) resonance reaction.

2.1.1 Cross section

The concept of a cross section is related to the probability that a nuclear reaction will occur. Classically, each nucleus has a geometrical area associated with it, that is proportional to the probability of interaction with target nuclei [10]. In this case, the cross section σ is obtained simply as

$$\sigma = \pi(R_{\mathrm{p}} + R_{\mathrm{t}})^2, \tag{2.1}$$

where R_{p} and R_{t} are the radii of the projectile and target nuclei respectively. Each radius can be estimated from

$$R = R_0 A^{1/3}, \tag{2.2}$$

where $R_0 = 1.2$ fm and A is the mass number. In actuality, since atomic nuclei are governed by the laws of quantum mechanics, the cross section depends on energy rather than a geometrical area. Therefore,

11

$$\sigma = \pi \lambdabar^2, \tag{2.3}$$

where $\lambdabar$ is the reduced de Broglie wavelength,

$$\lambdabar = \frac{m_{\rm p} + m_{\rm t}}{m_{\rm t}} \frac{\hbar}{(2m_p E_{\rm t})^{1/2}}. \tag{2.4}$$

Here $E_{\rm t}$ is the laboratory energy of the incident projectile with mass $m_{\rm p}$ and the mass of the target nucleus is $m_{\rm t}$.

2.1.2 Lorentzian widths of nuclear levels

The transition rate from an excited nuclear level is given by

$$\lambda = \frac{1}{\tau}, \tag{2.5}$$

where τ is the lifetime of the state. This can be expressed using Fermi's golden rule [23]

$$\frac{1}{\tau} = \frac{2\pi}{\hbar} |V_{\rm fi}|^2 \rho(E), \tag{2.6}$$

which can be arrived at by perturbation theory. Here V_{fi} is the matrix element for the transition, such that $V_{\rm fi} = \langle {\rm f} | H_{\rm int} | {\rm i} \rangle$, where $H_{\rm int}$ is the perturbing Hamiltonian and $\rho(E)$ is the density of available final states.

For the transitions to occur, it is essential to add an exponential decay term to the stationary state solution for the wave function of a given level. This is expressed as [24]

$$\psi(t) = \psi(0) \exp\left(-\frac{iE_0 t}{\hbar}\right) \exp\left(-\frac{\Gamma t}{2\hbar}\right). \tag{2.7}$$

Such a solution results in the familiar exponential decay after a time t

$$|\psi(t)|^2 = |\psi(0)|^2 \exp\left(-\frac{\Gamma t}{\hbar}\right), \tag{2.8}$$

and is attained by the addition of an imaginary attenuation factor to the energy [24]

12

$$E = E_0 - \frac{i\Gamma}{2}. \tag{2.9}$$

The above also shows that $\Gamma = \lambda\hbar$ or $\Gamma\tau = \hbar$. Here, Γ is the width of the state and τ is its lifetime. This equation shows that a finite width is essential for a transition to occur. In the limit $\tau \to \infty$ (stable states), $\Gamma \to 0$.

The shape of the state in the energy domain can be obtained from a Fourier transform to the time-dependent wave function in Eq. 2.7. Its normalized form results in a Breit-Wigner distribution

$$P(E) = \frac{\Gamma}{2\pi} \frac{1}{\left(E - E_0\right)^2 + \left(\frac{\Gamma}{2}\right)^2}, \tag{2.10}$$

also shown in Fig. 2.1, with central value E_a and width Γ_a. In general, a level has a total width Γ, that can be expressed as a sum of partial widths.

$$\Gamma = \Gamma_a + \Gamma_b + \Gamma_c..., \tag{2.11}$$

where a, b, c refer to different decay modes to various final states.
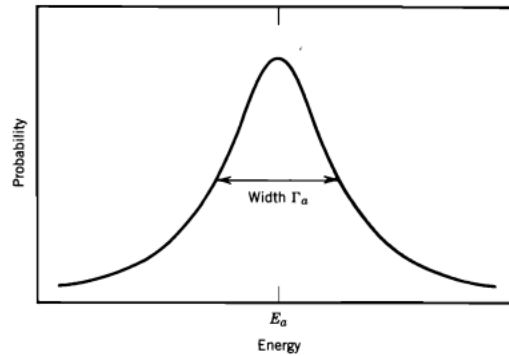
Figure 2.1: A Breit-Wigner distribution with width Γ_a.

2.2 Stellar reaction rates

As mentioned previously, nuclear cross sections are mainly energy dependent. Therefore, σ implicitly becomes a function of the relative velocity, v, between projectile and target nuclei. In a stellar environment, the velocities of particles are not monoenergetic. Instead the particles follow a velocity distribution $\phi(v)$. Thus, $\phi(v)dv$ is the probability that the relative velocity between interacting particles lies in the range v and

13

$v + dv$. Since the total number of reactions depends on the flux of the projectile nuclei, the number density of the target nuclei and the reaction cross section $\sigma(v)$, the reaction rate is proportional to $v\sigma(v)$ [5]. For a normalized probability density function $\phi(v)$, one can then define an averaged value [1]

$$\langle \sigma v \rangle = \int_0^\infty \phi(v)\sigma(v)vdv. \tag{2.12}$$

This is the average reaction rate per particle pair in a stellar environment. Further assuming that the stellar gas is in thermodynamic equilibrium, the nuclear velocities are assumed to follow a Maxwell-Boltzmann distribution. For interacting nuclei A and B, this is expressed as

$$\phi(v_A) = 4\pi v_A^2 \left(\frac{m_A}{2\pi kT}\right)^{3/2} \exp\left(-\frac{m_A v_A^2}{2kT}\right) \tag{2.13}$$

and

$$\phi(v_B) = 4\pi v_B^2 \left(\frac{m_B}{2\pi kT}\right)^{3/2} \exp\left(-\frac{m_B v_B^2}{2kT}\right). \tag{2.14}$$

Consequently, the average reaction rate per particle pair, $\langle \sigma v \rangle$ is simply [5]

$$\langle \sigma v \rangle = \int_0^\infty \int_0^\infty \phi(v_A)\phi(v_B)\sigma(v)vdv_A dv_B, \tag{2.15}$$

where v is the relative velocity between A and B.

The above is usually expressed in terms of the relative velocity v, the center of mass velocity V_{cm}, the reduced mass $\mu = \frac{m_A m_B}{m_A + m_B}$ and the total mass $M = m_A + m_B$, so that [5]

$$\langle \sigma v \rangle = \left(\frac{8}{\pi\mu}\right)^{1/2} \left(\frac{1}{kT}\right)^{3/2} \int_0^\infty \sigma(E)E \exp\left(-\frac{E}{kT}\right) dE. \tag{2.16}$$

The reaction rate in Eq. 2.16 is clearly dependent on the stellar temperature T. It is also evident from this equation that one needs to know the energy dependent cross section $\sigma(E)$ to evaluate a nuclear reaction rate. Below I will describe two types of reactions considered important to evaluate nuclear reaction rates in stars. Since this thesis pertains to a (p,γ) reaction rate, I shall only focus on charged-particle-induced reactions.

2.2.1 Non-resonant reactions

In nuclear reactions such as $^{20}\mathrm{Ne}(p,\gamma)$, where the projectile is a charged particle, the reaction is inhibited by the Coulomb barrier

---

[1]A relative velocity v between two particles is the same as one particle being at rest and the other moving with velocity v.

$$V_{\rm C} = \frac{Z_1 Z_2 e^2}{r}, \tag{2.17}$$

where $Z_1 e$ and $Z_2 e$ are the charges of the interacting nuclei and r is the separation distance between them. Together with the centrifugal (angular momentum) barrier, which goes as $\frac{\ell(\ell+1)}{r^2}$, the Coulomb barrier prevents rapid nuclear reactions in stars.

Despite the presence of such a barrier that prevents nuclear reactions at low energies, reactions still occur due to the phenomenon of quantum mechanical tunneling [25–27]. For example, for s-wave particles (with $\ell = 0$), with mass m, the transmission coefficient through the barrier at low energies is approximately

$$T \approx \exp\left(-\frac{2\pi}{\hbar}\sqrt{\frac{m}{2E}}Z_1 Z_2 e^2\right) \equiv \exp\left(-2\pi\eta\right), \tag{2.18}$$

where η is the Sommerfeld parameter

$$\eta = \frac{Z_1 Z_2 e^2}{\hbar v}. \tag{2.19}$$

This quantum tunneling probability T is also referred to as the Gamow factor [28, 29]. It is directly proportional to the cross section for charged-particle-induced nuclear reactions, so that

$$\sigma(E) \propto \exp(-2\pi\eta). \tag{2.20}$$

Furthermore, it has been already mentioned that

$$\sigma(E) \propto \pi\lambdabar^2 \propto 1/E. \tag{2.21}$$

Together, Eq. 2.20 and Eq. 2.21 can be expressed in a combined form as

$$\sigma(E) = \frac{1}{E}\exp(-2\pi\eta)S(E), \tag{2.22}$$

where $S(E)$ is the astrophysical S-factor. This S-factor contains the nuclear physics information not included in Eqs. 2.20 and 2.21. The S-factor for non-resonant reactions varies smoothly with energy, making it a useful tool in extrapolating the measured cross sections to astrophysical energies, from laboratory based experiments.

Substituting Eq. 2.22 into Eq. 2.16, one can arrive at [5]

$$\langle \sigma \nu \rangle = \left(\frac{8}{\pi \mu} \right)^{1/2} \left(\frac{1}{kT} \right)^{3/2} \int_0^\infty S(E) \exp \left[-\frac{E}{kT} - \frac{b}{E^{1/2}} \right] dE, \tag{2.23}$$

where

$$b = \frac{(2\mu)^{1/2} \pi e^2 Z_1 Z_2}{\hbar}. \tag{2.24}$$
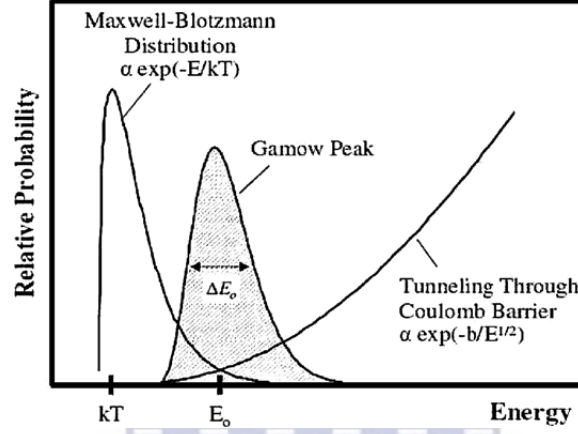
Figure 2.2: The Gamow peak, obtained from a convolution of the Maxwell-Boltzmann distribution and the penetrability factor of the Coulomb barrier. Figure taken from [30]

The convolution of the two terms in the integrand of Eq. 2.23 defines the Gamow window (in energy) where stellar nuclear reactions take place. This is shown in Fig. 2.2.

Figure 2.3 shows a non-resonant, direct capture reaction, expressed as $A(X, \gamma)B$. The projectile X is a plane wave of type $e^{i\vec{k}.\vec{r}}$, which forms a standing wave with orbital angular momentum quantum number ℓ in a compound nucleus B. This process results in the emission of photons with energy

$$E_\gamma = E + Q - E_i, \tag{2.25}$$

where E_i represents the energy eigenvalue of the level populated in B through the reaction. Since this is a single-step process, the cross section for this reaction is determined from the absolute squared value of the its matrix element,

$$\sigma(E) \propto |\langle B|H_\gamma|A + X \rangle|^2. \tag{2.26}$$

16
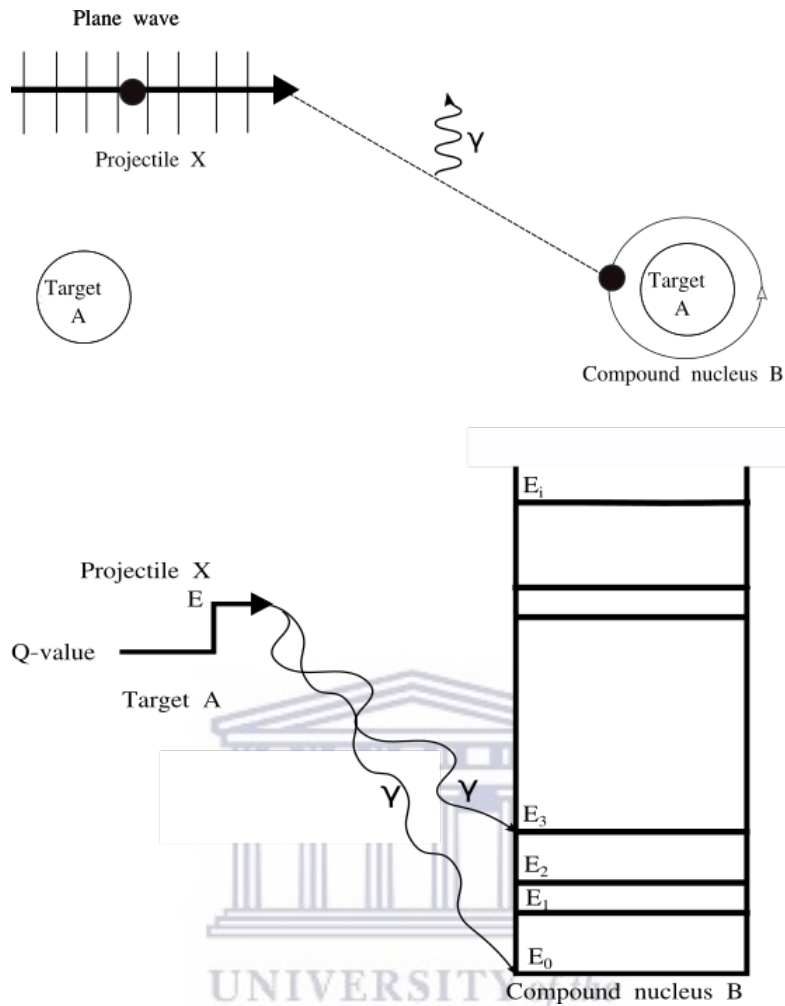
Figure 2.3: A direct (non-resonant) capture reaction of type $A(X, \gamma)B$.

2.2.2 Resonance reactions

Another class of reactions are resonance reactions, which occur when the kinetic energy of the projectile (in the center of mass frame) is such that the total energy in the incoming channel matches the energy of an excited nuclear state. Here [5]

$$E_R = E_i - Q, \tag{2.27}$$

where E_R is energy of the projectile X in the center of mass frame. This is shown pictorially as $A(X, \gamma)B$ in Fig. 2.4. This reaction only occurs at fixed energies when the above resonance condition is satisfied. The cross section of the reaction is significantly large at particular resonance values and is given by [10]

17

$$\sigma(E) \propto |\langle E_f | H_\gamma | E_i \rangle|^2 |\langle E_i | H_f | A + X \rangle|^2, \tag{2.28}$$

as a two-step process. In the above, the first matrix element corresponds to a γ-ray transition from $E_i \to E_f$, while the second corresponds to the production of a compound nuclear state with energy E_i, through the $A + x \to B$ resonance.
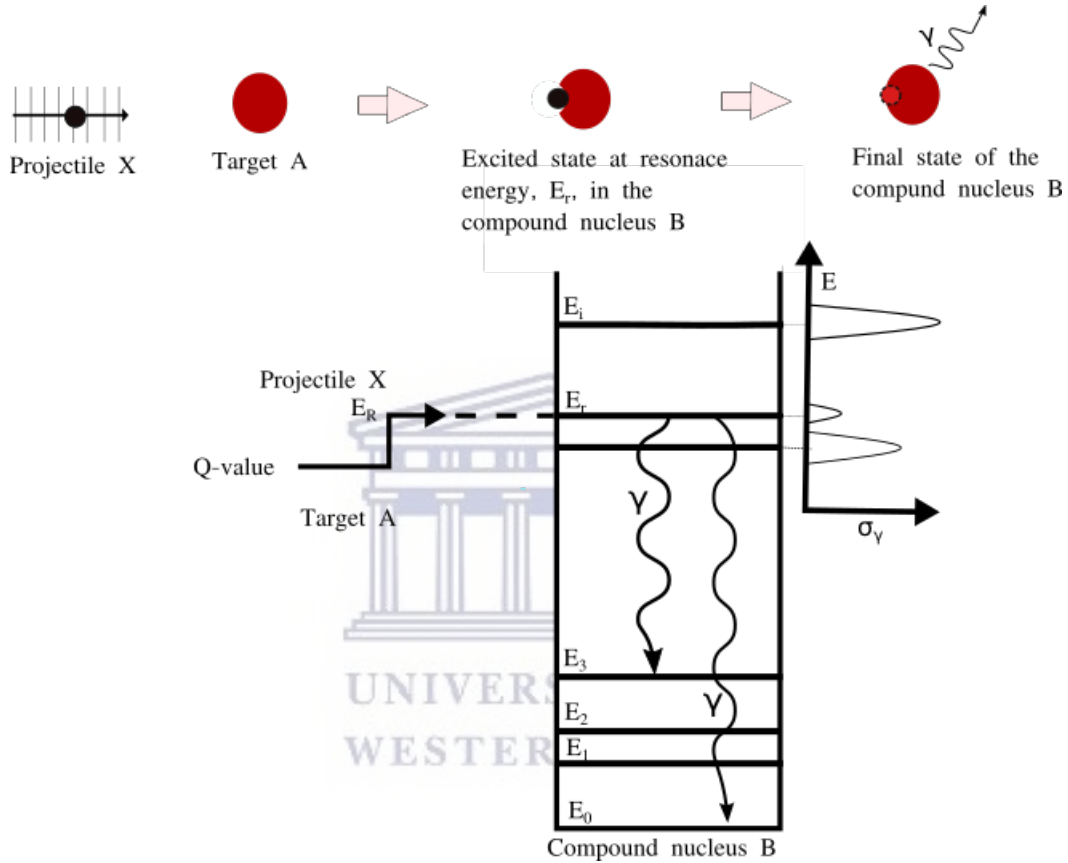
Figure 2.4: Pictorial description of a resonant capture reaction $A(X, \gamma)B$.

A derivation of the cross section for such resonance reactions can be obtained through an in-depth analysis of the scattering process. This is described below.

A general elastic scattering process can be schematically described as illustrated in Fig. 2.5. It consists of a plane wave incoming beam, scattering on a potential and outgoing as a spherical wave. At large distances (as $r \to \infty$) the total wave function is [10]

$$\psi_{\text{out}} = N \left[e^{(i\vec{k} \cdot \vec{r})} + f(\theta, \phi) \frac{e^{ikr}}{r} \right] \tag{2.29}$$

18
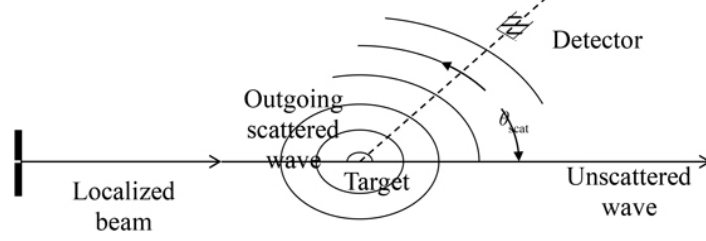
Figure 2.5: A typical scattering process on a potential, represented by a target.

In the above $f(\theta, \phi)$ is the scattering amplitude and contains the physics information relevant for the study. It is related to the differential scattering cross section, such that for a spherically symmetric potential (with no ϕ dependence)

$$\left(\frac{d\sigma}{d\Omega}\right) = |f(\theta)|^2. \tag{2.30}$$

It is often convenient to choose the quantization axis z along the direction of $\vec{k}$, so that

$$r\cos\theta = z, \tag{2.31}$$

which implies that

$$e^{i\vec{k}\cdot\vec{r}} = e^{ikz}. \tag{2.32}$$

Then the incoming plane waves with momentum $\hbar k$ can be expanded as [10]

$$e^{ikz} = \sum_{\ell=0}^{\infty}(2\ell+1)i^{\ell}j_{\ell}(kr)P_{\ell}(\cos\theta), \tag{2.33}$$

after separating the angular and radial parts of the wave function. Here $j_{\ell}(kr)$ are the spherical Bessel functions and $P_{\ell}(\cos\theta)$ are the Legendre polynomials.

At large values of r, a similar separation of variables and an expansion into the orthornormal eigenfunctions results in the right hand side of the below equation. The scattered wave function is affected by a phase shift δ_{ℓ}, on account of the potential at small r. Therefore, one obtains [31],

$$\sum_{\ell=0}^{\infty}(2\ell+1)i^{\ell}j_{\ell}(kr)P_{\ell}(\cos\theta) + f(\theta)\frac{e^{ikr}}{r} = \sum_{\ell=0}^{\infty}b_{\ell}R_{\ell}(kr)P_{\ell}(\cos\theta), \tag{2.34}$$

19

where

$$j_\ell(kr) = \frac{\sin(kr - \ell\pi/2)}{kr} \tag{2.35}$$

and

$$R_\ell(kr) = \frac{\sin(kr - \ell\pi/2 + \delta_\ell)}{kr}. \tag{2.36}$$

It is easy to show [31] that

$$b_\ell = (2\ell + 1)i^\ell e^{i\delta_\ell}, \tag{2.37}$$

and

$$f(\theta) = \frac{1}{k}\sum_{\ell=0}^{\infty}(2\ell+1)e^{i\delta_\ell}\sin(\delta_\ell)P_\ell(\cos\theta). \tag{2.38}$$

One can then use orthonormality of the Legendre polynomials, together with Eq. 2.30 and the fact that

$$\sigma = \int \left(\frac{d\sigma}{d\Omega}\right) d\Omega, \tag{2.39}$$

to obtain the final expression for the elastic scattering cross section

$$\sigma_{e\ell} = \frac{4\pi}{k^2}(2\ell+1)\sin^2\delta_\ell. \tag{2.40}$$

For a nuclear reaction, the scattering cross section can be obtained along the similar lines. Here the incoming particle number is not conserved as some of them react with the target nuclei. The incoming beam can be described by the current density

$$j_{\text{in}} = \frac{\hbar}{2mi}\left(\psi_{\text{in}}^*\nabla\psi_{\text{in}} - \nabla\psi_{\text{in}}^*\psi_{\text{in}}\right). \tag{2.41}$$

Therefore, for a plane wave of type e^{ikz}

$$j_{\text{in}} = \frac{\hbar k}{m}. \tag{2.42}$$

20

Since at $r \to \infty$, the total scattered wave function is

$$\psi_{\text{scat}} = \sum_{\ell=0}^{\infty} (2\ell+1)\, i^\ell e^{i\delta_\ell} \frac{\sin\left(kr - \ell\pi/2 + \delta_\ell\right)}{kr} P_\ell(\cos\theta), \tag{2.43}$$

its associated current density can be written as

$$j_{\text{scat}} = \frac{\hbar}{4mkr^2}\left[\left|\sum_{\ell=0}^{\infty}(2\ell+1)i^{\ell+1}e^{i\ell\pi/2}P_\ell(\cos\theta)\right|^2 - \left|\sum_{\ell=0}^{\infty}(2\ell+1)i^{\ell+1}e^{2i\delta_\ell}e^{-i\ell\pi/2}P_\ell(\cos\theta)\right|^2\right]. \tag{2.44}$$

This results in a cross section [10]

$$\sigma_{r,\ell} = \frac{\pi}{k^2}(2\ell+1)\left(1 - |e^{2i\delta_\ell}|^2\right), \tag{2.45}$$

again making use of the orthonormality of Legendre polynomials.

In the vicinity of a resonance one can simplify the formalism assuming:

- The existence of a nearly spherical nuclear surface at $r = R$, the nuclear radius.

- The projectile and the target do not interact at $r > R$.

One can then match the wave function and its derivative at this boundary [10], so that

$$u_\ell^{\text{in}}(R) = u_\ell^{\text{out}}(R), \tag{2.46}$$

$$\left(\frac{du_\ell^{\text{in}}(r)}{dr}\right)_{r=R} = \left(\frac{du_\ell^{\text{out}}(r)}{dr}\right)_{r=R}. \tag{2.47}$$

It is convenient at this point to introduce a dimensionless quantity called the logarithmic derivative

$$f_\ell \equiv R\left(\frac{1}{u_\ell(r)}\frac{du_\ell(r)}{dr}\right)_{r=R} = R\left(\frac{d\ln u_\ell(r)}{dr}\right)_{r=R} \tag{2.48}$$

The above aids in rewriting Eqs. 2.46 and 2.47 as

$$f_\ell(u_\ell^{\text{in}}) = f_\ell(u_\ell^{\text{out}}). \tag{2.49}$$

21

For simplicity, lets consider a *s*-wave resonance ($\ell = 0$). In the region $r > R$ the scattered wave function can be assumed to be

$$
\begin{aligned}
\psi_{\text{scat}} &= Ae^{ikr} + Be^{-ikr} \\
&= \frac{1}{kr}e^{i\delta_0}\sin(kr + \delta_0).
\end{aligned}
\tag{2.50}
$$

For $\ell = 0$ this is the same as the radial wave function

$$
\psi_{\text{scat}} = \frac{u_{\text{out}}(r)}{r}.
\tag{2.51}
$$

From Eqs. 2.51 and 2.48 it can be shown that

$$
e^{2i\delta_0} = \left(\frac{f_0 + ikR}{f_0 - ikR}\right)e^{-2ikR}.
\tag{2.52}
$$

Since f_0 is a complex quantity in general, it can be written as

$$
f_0 = g + ih.
\tag{2.53}
$$

Using Eqs. 2.45 and 2.52 the reaction cross section can now be rewritten as

$$
\begin{aligned}
\sigma_{\text{r},0} &= \frac{\pi}{k^2}\left(1 - \left|\frac{f_0 + iRk}{f_0 - iRk}e^{-2ikR}\right|\right)^2 \\
&= \frac{\pi}{k^2}\frac{-4kRh}{g^2 + (h - kR)^2}.
\end{aligned}
\tag{2.54}
$$

For $r \leq R$, the general solution of the wave function is of the type

$$
u_{\text{in}} = Ae^{iKr} + Be^{-iKr}.
\tag{2.55}
$$

Since the incoming particle is absorbed into the nuclear interior due to the formation of the compound nucleus, the amplitude of the outgoing spherical wave will be much smaller than that of the incoming wave. It is assumed that [10]

$$
A = Be^{2i\xi}e^{-2q}.
\tag{2.56}
$$

22

Then one obtains

$$u_{in} = 2B \cos\left(Kr + \xi + iq\right)e^{i\xi - q}. \tag{2.57}$$

This results in

$$f_0 = -RK \tan\left(KR + \xi + iq\right). \tag{2.58}$$

Since reaction cross sections are enhanced at resonance energies, the wave functions' amplitudes within $r \leq R$ have to be maximal. This implies that the slope of the radial wave function has to be zero at $r = R$. Thus, one can define a set of resonance energies E_λ using the condition

$$f_0(E_\lambda, q) = -KR \tan\left(KR + \xi + iq\right) = 0. \tag{2.59}$$

Expanding $f_0(E, q)$ about $E_\lambda = 0$ and $q = 0$ yields

$$f_0 \approx f_0(E_\lambda, q) + (E - E_\lambda)\left(\frac{\partial f_0}{\partial E}\right)_{E_\lambda, q=0} + q\left(\frac{\partial f_0}{\partial q}\right)_{E_\lambda, q=0}, \tag{2.60}$$

which is easily simplified to

$$f_0 = (E - E_\lambda)\left(\frac{\partial f_0}{\partial E}\right)_{E_\lambda, q=0} - iqKR. \tag{2.61}$$

Substituting the above into Eq. 2.54, the cross section reduces to

$$\sigma_{r,0} = \frac{\pi}{k^2} \frac{\frac{(2kR)(qKR)}{(\partial f_0 / \partial E)^2_{E_\lambda, q=0}}}{(E - E_\lambda)^2 - \frac{(qKR + kR)^2}{(\partial f_0 / \partial E)^2_{E_\lambda, q=0}}}. \tag{2.62}$$

One can then make use of the following definitions [10]

$$\Gamma_{\lambda e} \equiv \frac{-2kR}{(\partial f_0 / \partial E)_{E_\lambda, q=0}}, \tag{2.63}$$

and

$$\Gamma_{\lambda r} \equiv \frac{-2qKR}{(\partial f_0 / \partial E)_{E_\lambda, q=0}}, \tag{2.64}$$

where Γ_λ (the total width) is the sum of the particle width $\Gamma_{\lambda e}$ and the reaction width $\Gamma_{\lambda r}$, so that

23

$$\Gamma_\lambda = \Gamma_{\lambda e} + \Gamma_{\lambda r}. \tag{2.65}$$

The above formalism can be extended to charged particles for different values of ℓ

$$\sigma_{r,\ell}(E) = (2\ell + 1)\frac{\pi}{k^2}\frac{\Gamma_{\lambda e}\Gamma_{\lambda r}}{(E - E_\lambda)^2 + \Gamma_\lambda^2/4}. \tag{2.66}$$

It may be noted that the right hand side of the above equation has the familiar form of a Breit Wigner (Lorentzian) function, defined previously in Eq. 2.10.

A generalized formula of the Breit Weigner cross section σ_{BW}, involving charged or neutral particles with spins is then

$$\sigma_{BW}(E) = \frac{\pi}{k^2}\omega\frac{\Gamma_{\lambda e}\Gamma_{\lambda r}}{(E - E_\lambda)^2 + \Gamma_\lambda^2/4}, \tag{2.67}$$

where ω is the statistical factor $\frac{(2J+1)}{(2S_\mathrm{p}+1)(2S_\mathrm{t}+1)}$, and S_p, S_t are the spins of the projectile and the target nuclei. The resonance strength for the reaction is defined as [5]

$$\omega\gamma = \omega\frac{\Gamma_{\lambda e}\Gamma_{\lambda r}}{\Gamma_\lambda}. \tag{2.68}$$

Substituting Eq. 2.67 into Eq. 2.16 one obtains reaction rate over the resonance energy E_λ

$$\langle\sigma v\rangle = \left(\frac{8}{\pi\mu}\right)^{1/2}\left(\frac{1}{kT}\right)^{3/2}\int_0^\infty \sigma_{BW}(E)E\exp\left(-\frac{E}{kT}\right)dE. \tag{2.69}$$

Integrating the Breit Wigner cross section over E_λ, the reaction rate takes its final form

$$\langle\sigma v\rangle = \left(\frac{2\pi}{\mu}\right)^{3/2}\left(\frac{1}{kT}\right)^{3/2}\hbar^2\omega\gamma\exp\left(-\frac{E_\lambda}{kT}\right). \tag{2.70}$$

Eq 2.70 makes it is evident that the reaction rate is proportional to the resonance strength, $\omega\gamma$.

24

2.3 Electromagnetic transitions between nuclear levels

Excited states that are produced by resonance reactions such as $A(X, \gamma)B$ can decay by particle and γ radiation. The latter is usually produced via cascading (or direct) transitions to the ground state of the nucleus B. The individual γ-rays have certain multipolarity, described below.

To better understand electromagnetic (EM) transitions in nuclei, it is important to consider that the charge distributions generate EM fields and currents. The many-body nuclear system ends up interacting with the fields.

Starting with the wave equation for a vector potential [32]

$$\nabla^2 \vec{A} - \frac{1}{c^2} \frac{\partial^2 \vec{A}}{\partial t^2} = 0, \tag{2.71}$$

it is well known that this partial differential equation has plane wave solutions of the type

$$\vec{A}(\vec{r}, t) = \vec{A}_0 e^{i(\vec{k}.\vec{r} - \omega t)}. \tag{2.72}$$

Assuming periodic boundary conditions in a cavity of volume L^3, with $\vec{k}$ taking discrete values, the most general solution to the wave equation is [33]

$$A(\vec{r}, t) = \frac{1}{L^{3/2}} \sum_{\vec{k}, \lambda} \left[C_{\vec{k}, \lambda} \widehat{\epsilon}(\vec{k}, \lambda) e^{i(\vec{k}.\vec{r} - \omega t)} + C_{\vec{k}, \lambda}^* \widehat{\epsilon}(\vec{k}, \lambda) e^{-i(\vec{k}.\vec{r} - \omega t)} \right], \tag{2.73}$$

where the vectors $\widehat{\epsilon}(\vec{k}, \lambda)$ indicate the polarization of $\vec{A}$ for each $\vec{k}$. In order to quantize the radiation field, the above solution is replaced by the operator

$$\vec{A} = \frac{1}{L^{3/2}} \sum_{\vec{k}, \lambda} c \sqrt{\frac{\hbar}{2\omega}} \left[a_{\vec{k}, \lambda} \widehat{\epsilon}(\vec{k}, \lambda) e^{i(\vec{k}.\vec{r} - \omega t)} + a_{\vec{k}, \lambda}^{\dagger}{}^* \widehat{\epsilon}(\vec{k}, \lambda) e^{-i(\vec{k}.\vec{r} - \omega t)} \right], \tag{2.74}$$

where $a_{\vec{k}, \lambda}^{\dagger}$ and $a_{\vec{k}, \lambda}$ are the usual creation and annihilation operators and the EM Hamiltonian is

$$\widehat{H}_{\text{EM}} = \sum_{\vec{k}, \lambda} \hbar \omega \left(a_{\vec{k}, \lambda}^{\dagger} a_{\vec{k}, \lambda} + \frac{1}{2} \right). \tag{2.75}$$

The above prescription takes into account both absorption as well as emission of photons.

25

On the other hand, the interaction Hamiltonian for a spin-$\frac{1}{2}$ particle with mass m and charge q in an EM field is given by [24]

$$H_{\text{int}} = \frac{1}{2m} \left(\vec{p} - \frac{q\vec{A}}{c} \right)^2 + q\phi - \frac{q\hbar}{2m}\vec{\sigma}.\vec{B} \ , \tag{2.76}$$

where the magnetic moment is defined as

$$\vec{\mu} = \frac{q\hbar}{2m}\vec{\sigma}. \tag{2.77}$$

Therefore, EM transition rates in nuclei can be obtained from Fermi's golden rule (with a similar H_{int} for a system of nucleons) and the operator expansion in Eq. 2.74 for the vector potential $\vec{A}$ that involves the creation operator $a^{\dagger}_{\vec{k},\lambda}$.

The EM radiation emitted from excited state in nuclei are classified by multipole orders L, depending on the angular momentum taken away by the photons. When the charge distribution within a nucleus couples with the $\vec{E}$ field, it induces an electric transition. On the other hand, the orbital motion of the protons lead to magnetic transitions. The selection rules of electric and magnetic transitions of multipole order L are such that, for a transition between an initial state with spin-parity $J_{\text{i}}^{\pi_{\text{i}}}$ and a final state with spin-parity $J_{\text{f}}^{\pi_{\text{f}}}$, the multipolarity of the radiation is in the range

$$|J_{\text{f}} - J_{\text{i}}| \leq L \leq J_{\text{f}} + J_{\text{i}}.$$

The parity selection rule is as follows

$$\pi_{\text{i}}\pi_{\text{f}} = (-1)^L \quad \text{for} \quad E(L) \quad \text{transitions} \tag{2.78}$$

and

$$\pi_{\text{i}}\pi_{\text{f}} = (-1)^{L+1} \quad \text{for} \quad M(L) \quad \text{transitions.} \tag{2.79}$$

In general, the lowest multipolarity dominates and magnetic transitions are weaker than the electric ones. In some transitions involving $E(L+1)$ and $M(L)$ matrix elements, their strengths can be comparable. In such cases it is customary to define a mixing ratio from the ratio of measured transition rates

$$\delta^2 = \frac{W(E(L+1))}{W(M(L))}. \tag{2.80}$$

26

This mixing ratio δ relates $E2$ and $M1$ matrix elements. In general, a transition probability for a multipole L is given by [34]

$$W(L, J_\mathrm{i} \to J_\mathrm{f}) = \frac{8\pi (L+1) k^{2L+1}}{L [(2L+1)!!]^2 \hbar} B(L, J_\mathrm{i} \to J_\mathrm{f}), \tag{2.81}$$

where the transition strength is

$$B(L, J_\mathrm{i} \to J_\mathrm{f}) = \frac{1}{2J_\mathrm{i}+1} |\langle J_\mathrm{f}||O_L||J_\mathrm{i}\rangle|^2, \tag{2.82}$$

with $|\langle J_\mathrm{f}||O_L||J_\mathrm{i}\rangle|$ being the reduced matrix element for the transition and $\hat{O}_L$ being the transition operator.

2.4 The angular distribution of γ-rays following resonant capture

Consider an initial resonant state represented by $|J_1 M_1\rangle$ that de-excites to a final state $|J_2 M_2\rangle$ via the emission of a γ-ray. The transition probability for a photon with wave number $\vec{k}$ and polarisation $\vec{\epsilon}$ is given by Fermi's golden rule [35]

$$\frac{1}{\tau} = \frac{1}{2\pi\hbar} \left| \langle J_1 M_1 | H(\vec{k}, \vec{\epsilon}) | J_2 M_2 \rangle \right|^2. \tag{2.83}$$

The interaction Hamiltonian $H(\vec{k}, \vec{\epsilon})$, that causes this transition is of the form given by Eq. 2.76, where $\vec{A}$ satisfies the vector wave equation (Eq. 2.71). The solutions to this equation are the sets of vector fields $\vec{\nabla}\phi_{LM}$, $\vec{L}\phi_{LM}$ and $\vec{\nabla} \times \vec{L}\phi_{LM}$ usually expressed in their normalized forms [36,37]

$$\begin{aligned}
\vec{A}_{LM} &= (ik)^{-1}\vec{\nabla}\phi_{LM}, \\
\vec{A}^e_{LM} &= \{k[L(L+1)]^{1/2}\}^{-1}\vec{\nabla} \times \vec{L}\phi_{LM}, \\
\vec{A}^m_{LM} &= \{[L(L+1)]^{1/2}\}^{-1}\vec{L}\phi_{LM}.
\end{aligned} \tag{2.84}$$

In the above, the ϕ_{LM} include both the radial and angular solutions and the superscripts 'e' and 'm' label the electric and magnetic multipole components of the transverse field. The first solution is the longitudinal solution and not required to be expanded into plane EM waves.

A given circularly polarized transverse plane wave, with polarization vectors $\hat{e}_{+1}$ and $\hat{e}_{-1}$ for left and right circular polarizations, can be expressed as a plane wave expansion

27

$$\hat{e}_q \exp\left(ikz\right) = -\frac{1}{\sqrt{2}} \sum_L \left(q\vec{A}_{Lq}^m + \vec{A}_{Lq}^e \right), \tag{2.85}$$

whose most general form is

$$\hat{e}_q \exp\left(i\vec{k}.\vec{r}\right) = -\frac{1}{\sqrt{2}} \sum_{LM} \left(q\vec{A}_{LM}^m + \vec{A}_{LM}^e \right) \mathfrak{D}_{M_q}^L(R), \tag{2.86}$$

where $\mathfrak{D}_{M_q}^L(R)$ is a rotation matrix [32] that generates a rotation R in the direction of the wave vector $\vec{k}$.

In a more compact notation [36], this is written as

$$\hat{e}_q \exp\left(i\vec{k}.\vec{r}\right) = -\frac{1}{\sqrt{2}} \sum_{LM\pi} q^\pi \vec{A}_{LM}^\pi \mathfrak{D}_{M_q}^L(R) \tag{2.87}$$

where 'π' labels the electric ($\pi = 0$) or magnetic ($\pi = 1$) nature of the fields.

The radial and angular solutions of the wave equation (Eq. 2.71) are of the form $j_L(kr)$ (spherical Bessel functions) and $Y_L^M(\theta, \phi)$ (spherical harmonics). In the long-wavelength approximation ($kr \ll 1$), the above plane-wave expansion results in a more simplified version of the EM Hamiltonian [36, 37]

$$H_{int}(\vec{k}, \vec{\epsilon}_q) = -\sum_{LM\pi} q^\pi T_{LM}^\pi \mathfrak{D}_{M_q}^L(R), \tag{2.88}$$

which results in the matrix element

$$-\sum_{LM\pi} q^\pi \mathfrak{D}_{M_q}^L(R) \langle J_2 M_2 | T_{LM}^\pi | J_1 M_1 \rangle$$

for an EM transition.

In the above, the electric and magnetic operators T_{LM}^π represent the interaction multipole operators [36] and are expressed by combinations of the radial and angular solutions of the wave equation. In the long-wavelength limit, the radial part reduces to a simple r^L dependence [36].

Next, defining $w(M_1)$ to be the population parameters that represent the relative population of the substates labeled by M_1, the transition probability for a cylindrically symmetric case is

$$P^q(\vec{k}) = \sum_{M_1} w(M_1) \sum \frac{k}{2\pi\hbar} q^\pi q^{\pi'} \mathfrak{D}_{M_{q'}}^{L'*}(R) \mathfrak{D}_{M_q}^L(R) \times \langle J_2 M_2 | T_{LM}^\pi | J_1 M_1 \rangle \langle J_2 M_2 | T_{LM}^{\pi'} | J_1 M_1 \rangle^*. \tag{2.89}$$

28

Further using the Wigner-Eckart theorem [36], the symmetry of the $\mathfrak{D}$ matrices, and the fact that $\mathfrak{D}_{00}^k = P_K(\cos\theta)$, the transition probability reduces to

$$P^q(\mathbf{k}) = \left(\frac{k}{2\pi\hbar}\right) \sum_{KLL'\pi\pi'} B_K(J_1) R_K^q(LL'J_1J_2) P_K(\cos\theta) q^{\pi+\pi'} \frac{\langle J_1||T_{LM}^{\langle\pi\rangle}||J_2\rangle}{(2L+1)^{1/2}} \frac{\langle J_1||T_{LM}^{\langle\pi'\rangle}||J_2\rangle^*}{(2L'+1)^{1/2}}. \tag{2.90}$$

Here the $R_K^q(LL'J_1J_2)$ coefficients are [36]

$$R_K^q(LL'J_1J_2) = (-)^{q+J_1-J_2+L'-L-K}(2J_1+1)^{1/2}(2L+1)^{1/2}(2L'+1)^{1/2}\langle LL'q-q|K0\rangle W(J_1J_1LL';KJ_2), \tag{2.91}$$

and $W(J_1J_1LL';KJ_2)$ is the Racah W-coefficient

$$W(J_1J_1LL';KJ_2) = (-)^{L+L'+2J_1} \begin{Bmatrix} L & J_1 & J_2 \\ J_1 & L' & K \end{Bmatrix}. \tag{2.92}$$

The $B_k(J_1)$ terms are the statistical tensors

$$B_k(J_1) = \sum_{M_1} w(M_1)(-)^{J_1-M_1}(2J_1+1)^{1/2}\langle J_1J_1M_1-M_1|K0\rangle. \tag{2.93}$$

If the circular polarization is not observed, and the initial state is aligned such that

$$w(-M_1) = w(M_1), \tag{2.94}$$

one can revert back to the definition of a mixing ratio for the two lowest multipolarities of the transition

$$\delta = \frac{\langle J_1||T_{L'}^{\langle\pi\rangle}||J_2\rangle/(2L'+1)^{1/2}}{\langle J_1||T_L^{\langle\overline{\pi}\rangle}||J_2\rangle/(2L+1)^{1/2}}, \tag{2.95}$$

to express the transition probability in a more simple form

$$P^q(\mathbf{k}) = \left(\frac{k}{2\pi\hbar}\right) \sum_{KLL'\pi\pi'} B_K(J_1) R_K^q(LL'J_1J_2) P_K(\cos\theta) q^{\pi+\pi'} \frac{\langle J_1||T_{LM}^{\langle\pi\rangle}||J_2\rangle}{(2L+1)^{1/2}} \frac{\langle J_1||T_{LM}^{\langle\pi'\rangle}||J_2\rangle^*}{(2L'+1)^{1/2}}. \tag{2.96}$$

The alignment condition in Eq. 2.94 assures that only $K =$ even contribute, since $B_k(J_1) = 0$, when K takes odd values.

29

This formalism shows that one can obtain a mixing ratio δ from a measured angular distribution about the symmetry axis

$$W(\theta) = \sum_{K=\text{even}} \frac{B_K(J_1)R_K(LL'J_1J_2)\delta_L^\pi \delta_{L'}^{\pi'} P_K(\cos\theta)}{\sum_L |\delta_L^\pi|^2}. \tag{2.97}$$

If only the two lowest multipoles L and L' contribute, then the angular distribution is simply

$$W(\theta) = \sum_{K=\text{even}} B_K(J_1)P_K(\cos\theta) \left[\frac{R_K(LLJ_1J_2) + 2\delta R_K(LL'J_1J_2) + \delta^2 R_K(L'L'J_1J_2)}{(1+\delta^2)} \right]. \tag{2.98}$$

Resonant capture results in an excited compound nuclear state with definite angular momentum and parity. In the case of a (p,γ) reaction, the proton can carry different values of orbital angular momentum ℓ. Together with the spins of the target and the projectile, the ℓ value of the incoming proton contributes to the formation of the final state of the excited nucleus. If one takes the axis of symmetry to be about the beam axis, the channel spin s couples with ℓ (with $m_\ell = 0$) to form the state labeled by $|J_1M_1\rangle$.

In such a situation, the population parameters are simiply [36]

$$w(M_1) = \langle sJ_1M_1 - M_1|\ell 0\rangle^2. \tag{2.99}$$

If more than one channel spin contribute, then the contributions add incoherently, with each contribution $T(s)$, so that

$$w(M_1) = \sum_s \langle sJ_1M_1 - M_1|\ell 0\rangle^2 T(s), \tag{2.100}$$

with $\sum_s T(s) = 1$. Under such circumstances, the $B_k(J_1)$ alignment coefficients are

$$B_k(J_1) = \sum_s (-)^{s-J_1}[((2L+1)^{1/2})]^2(2J_1+1)^{1/2}\langle ll00|K0\rangle W(J_1J_1ll;Ks)T(s). \tag{2.101}$$

2.5 The case of $^{20}\text{Ne}(p,\gamma)$

Figure 2.6 shows the astrophysically important resonance related to this work. As mentioned in Section 1.1, the 3544.3 keV resonance at $E_p^{\text{c.m.}} = 1113$ keV is the dominant contribution to the $^{20}\text{Ne}(p,\gamma)$ reaction rate at high temperatures. In addition, the non-resonant (direct capture) to the 2424 and 332 keV states also significantly contribute to the total reaction rate. These aspects were comprehensively studied earlier, by
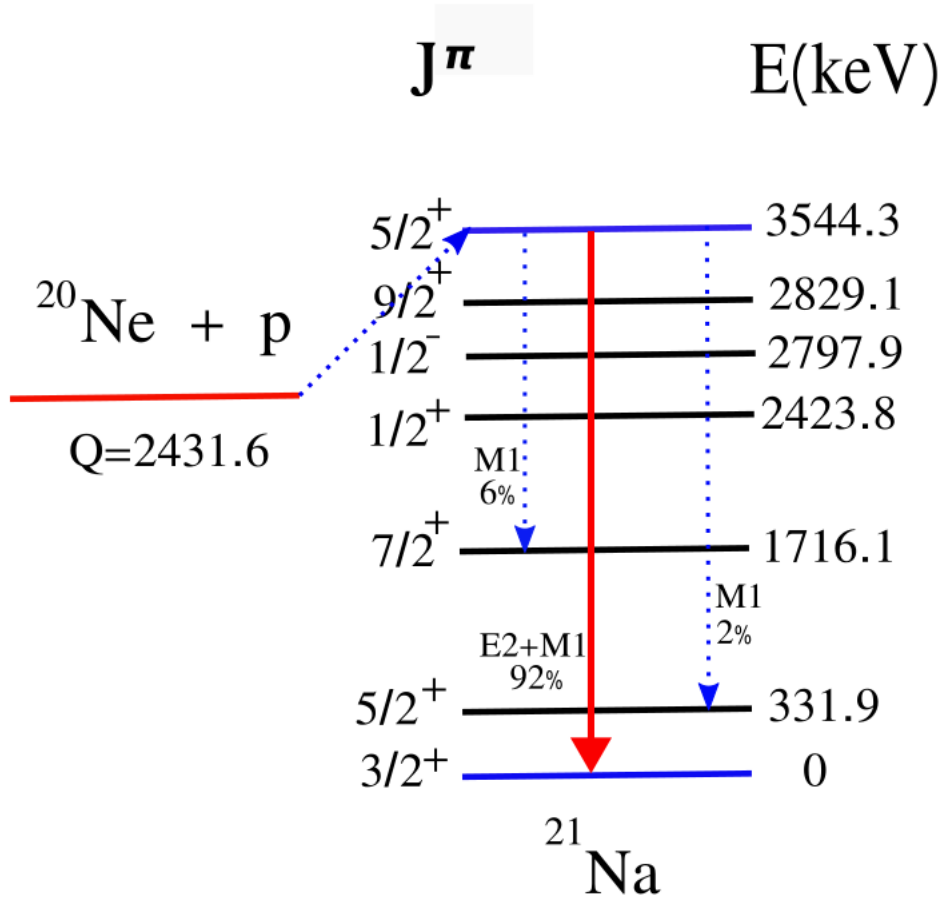
Figure 2.6: The $^{20}\text{Ne}(p, \gamma)^{21}\text{Na}$ resonance and the transition of interest from the 3544.3 keV to the ground state in ^{21}Na.

Rolfs *et al.* [22] and Lyons *et al.* [1]. Reference [22] studied the resonance contributions over the proton energy range $0.4 \leq E_p \leq 2.1$ MeV, while the latter obtained excitation function data over a proton energy range of $0.5 \leq E_p \leq 2.0$ MeV. In both cases, cross sections were measured using extended gas targets. Due to the non-localized nature of the source of the γ-rays in both experiments, the cross sections were determined relative to the narrow $5/2^+$ resonance state at 3544.3 keV, which has a total width of $\Gamma = 15.5(14)$ eV [38] and a measured resonance strength, $\omega\gamma = 0.94(4)$ eV [1].

Since the 3544.3 keV state in ^{21}Na decays to the ground state for the majority of the time (with 92% absolute branch), the 3544.3 keV γ-ray was used to measure the resonance strength using the relation

$$\omega\gamma = \frac{2}{\lambda_R^2} \frac{1}{n} \frac{1}{B\eta W(\theta)} \int \frac{N(E_0)}{N_{\text{beam}}} dE_0, \tag{2.102}$$

31

where λ_R^2 is the de Broglie wavelength at the resonance energy, n is the number of target nuclei, B is the branching ratio of the transition observed, η is the detector efficiency and $W(\theta)$ is the angular distribution for the 3544.3 keV γ-rays. The integral was performed over the width of the resonance. Because of the diffuse nature of the gas targets, the authors of both Refs. [1, 22] independently used implanted ^{20}Ne target to measure the resonance strength for this particular state in the above manner.

Once the $\omega\gamma$ for the 3544.3 keV resonance was measured, in the direct capture and the resonant contributions to the reaction rate were determined in both experiments using [1]

$$\sigma_{\mathrm{R/DC}} = \frac{\lambda_R^2}{2} \frac{m+M}{m} \frac{\omega\gamma}{\Delta E} \frac{Y_{\mathrm{R/DC}}}{Y_{1113}},\qquad(2.103)$$

where

$$\frac{Y_{\mathrm{R/DC}}}{Y_{1113}} = \frac{N_{\mathrm{R/DC}}}{N_{1113}} \frac{\epsilon_{1113}}{\epsilon_{\mathrm{R/DC}}} \frac{\Omega_{1113}}{\Omega_{\mathrm{R/DC}}} \frac{W(\theta)_{1113}}{W(\theta)_{\mathrm{R/DC}}}.\qquad(2.104)$$

Here m and M are the projectile and target masses and ΔE is the target thickness. The subscript "1113" represents the 1113 keV resonance, while "R/DC" includes the resonant and direct capture components. The yield ratio in Eq 2.104, includes ratios of counts ($N_{\mathrm{R/DC}}/N_{1113}/$), stopping powers ($\epsilon_{1113}/\epsilon_{\mathrm{R/DC}}$), solid angles ($\Omega_{1113}/\Omega_{\mathrm{R/DC}}$) and angular distributions ($W(\theta)_{1113}/W(\theta)_{\mathrm{R/DC}}$).

It is important to note at this point that both of these (independent) experiments relied on a previously measured angular distribution for the 3544.3 $\rightarrow$ 0 keV transition (see Fig. 9 in Ref. [1]). The E2/M1 mixing ratio for this transition $\delta = 0.07(2)$, was measured nearly 60 years ago using NaI scintillator detectors [4]. This value was implicit in the analysis of Refs. [1, 22] to determine the ^{20}Ne(p, γ) reaction rate. In light of the above, this project aimed to remeasure the mixing ratio for this transition, using higher resolution High-Purity Germanium (HPGe) detectors.

32

Chapter 3

Experimental details

3.1 Facility

The experiment was performed in the summer of 2019 at the Center for Experimental Nuclear Physics and Astrophysics (CENPA) at the University of Washington in Seattle, USA. The facility houses a High Voltage Engineering FN tandem Van de Graaff accelerator, which is shown in Fig. 3.1.

Usual tandem operation requires a negatively charged low-energy beam of ions accelerated towards a positively charged terminal at several million volts. Following this first stage of acceleration, the ions are stripped of their electrons using either a carbon foil or a gas stripper. A second stage of acceleration is imposed on account of these positive ions being repelled from the positive terminal voltage. However, for this particular experiment, this standard approach of the tandem operation was not used and certain modifications were made. The device was reconfigured as a single-ended machine, with a Radio Frequency (RF) positive ion-source located at the terminal. The high energy FN beam tube was replaced by a modified KN-type beam tube, which allowed a different field gradient for a higher intensity beam. The terminal ion source (TIS) had a pressurized H_2 gas bottle, together with an einzel lens, magnetic steerers and a small permanent dipole bending magnet [40].

To obtain a high intensity proton beam, hydrogen gas was bled slowly into the source cavity that was surrounded by RF coils. The oscillatory RF field caused the electrons to move in a spiral motion, thereby ionizing the gas within the volume. A voltage of about 10 kV was used to extract the H^+ ions from the source, with the aid of the electromagnetic steering and focusing units mentioned above. The TIS enabled a high-intensity ($\sim 50~\mu A$) and low-energy proton beam to produce the $^{20}Ne(p,\gamma)$ resonance of interest. It

33
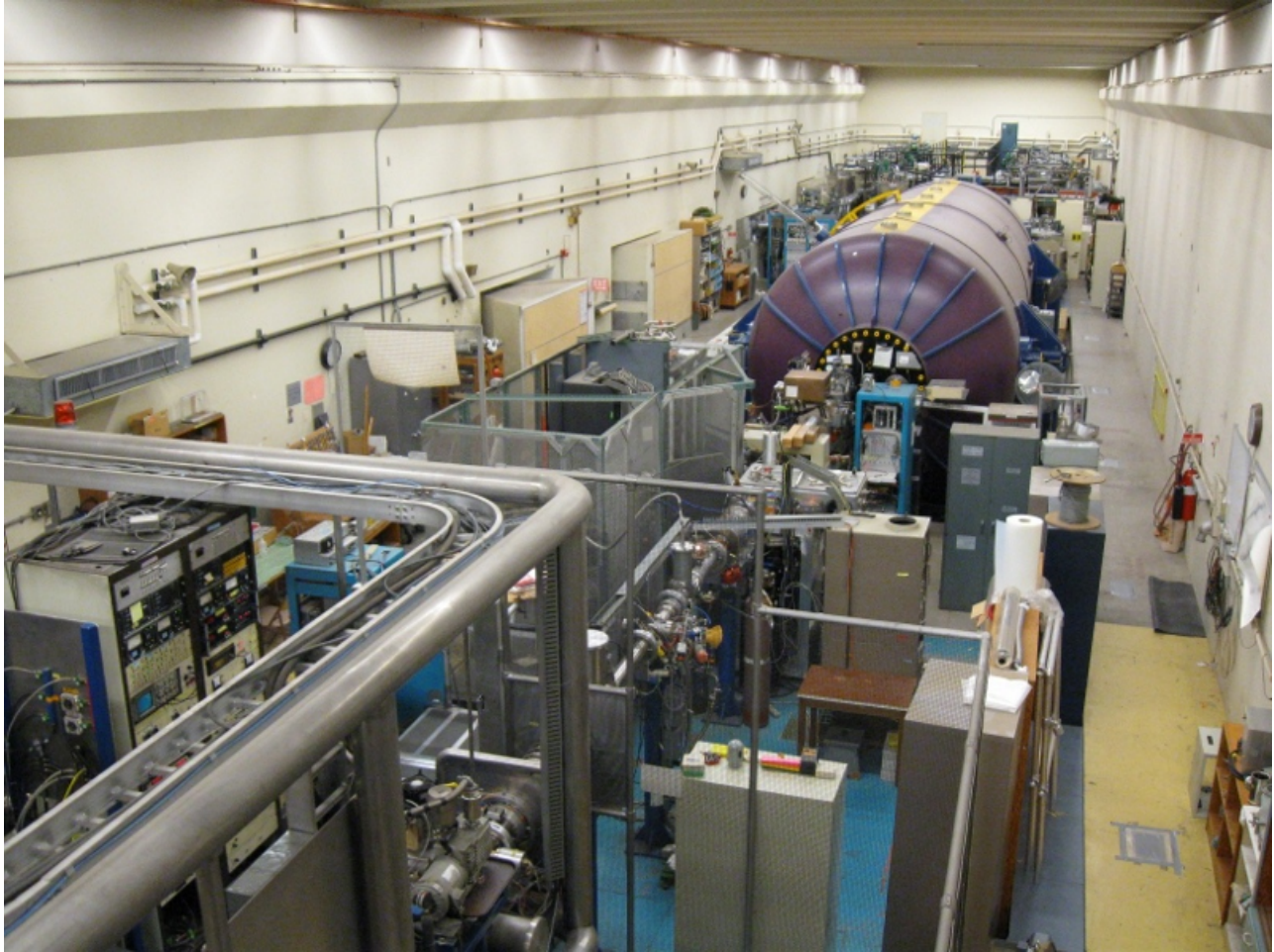
Figure 3.1: Tandem accelerator facility at CENPA. Picture taken from Ref [39].

also allowed for a simultaneous preparation of other implanted neon targets during the same beam time. The target implantation was performed downstream of the low-energy injector deck to the tandem, which was available because of the TIS mode of operation. This was important for replacing targets during the course of the experiment, as the high intensity beam degraded the implanted targets rather quickly.

3.2   Target preparation

The ^{20}Ne targets were prepared by implanting a 90 keV ^{20}Ne^{2+} beam onto 1-mm-thick 99.98 % pure tantalum foils. The ion source used to produce the ^{20}Ne^{2+} beams was a simple Direct Extraction Ion Source (DEIS). A neon gas bottle placed at the source was used to produce the ion beam. The DEIS worked on the simple operating principle of an arc-discharge between a hot cathode filament and the anode terminal of the source, that forms a plasma within the confined region of the anode. Generally an applied potential difference of

34

around of 100 V is enough to extract an ion-beam. For this experiment a positive ion-beam was produced from the core of positive ions within the plasma. The beam was extracted and guided using several steering and focusing elements. An implantation region, separated from the rest of the ion-optics by a liquid N_2 cold trap was located near the low-energy end of the accelerator. This implantation chamber was used to make several ^{20}Ne targets during the course of the experiment. The targets were observed to saturate at areal densities of around 20 μg/cm^2.

3.3   Experimental procedure

The implanted target was placed in a water-cooled target chamber. A schematic of this chamber is shown in Fig. 3.2, along with a photograph shown in Fig. 3.3. A description of the target chamber can be found in Ref. [41]. Five HPGe detectors were used for the angular distribution measurement. These included two two-fold segmented Eurisys Mesures clover detectors, two Canberra detectors with 100% relative efficiency and an ORTEC detector with 80% relative efficiency. Figures 3.4 and 3.5 show photographs of the actual detector set up. Table 3.1 lists the positions of the detectors with respect to the beam direction and the target. To prevent coincidence summing of cascading γ rays, 1 cm thick Pb shields were placed in front of each detector. Beam events were scaled using a Brookhaven Instruments Corporation (BIC) current integrator that was coupled to a LeCroy 2551 Scaler. Standard NIM and CAMAC electronics were used for the data acquisition. The energy and timing signals from the HPGe detectors were obtained from ORTEC 572 amplifiers and 474 Timing Filter Amplifiers (TFAs). The signals were digitized using ORTEC 413A analog-to-digital converter (ADCs) and a Fast Encording and Readout ADC (FERA) and saved event-by-event in full list mode for future analysis.

The detectors were calibrated using ^{56}Co and ^{60}Co γ-ray sources placed at the central location of the target foil. The activities of these sources were around 3.7 kBq and 8 kBq respectively. The calibration data were acquired both before and after the ^{20}Ne(p,γ) runs. For the ^{20}Ne(p,γ) data, the energy of the resonance was determined by scanning the proton beam over an energy range 1164 keV $\leq E_p \leq$ 1182 keV. Registered γ-ray information was used to plot a γ-ray excitation function for the 3.5 MeV γ-ray, over the proton's energy range. A sample yield curve from one detector is shown in the Fig. 3.6.
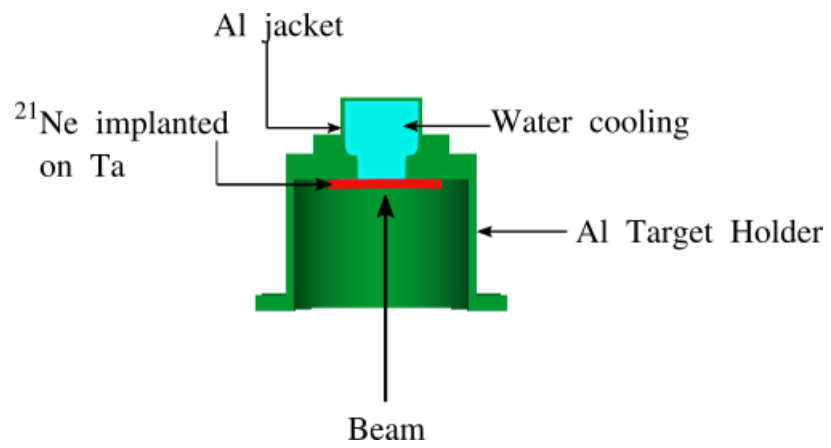
Figure 3.2: Target holder arrangement
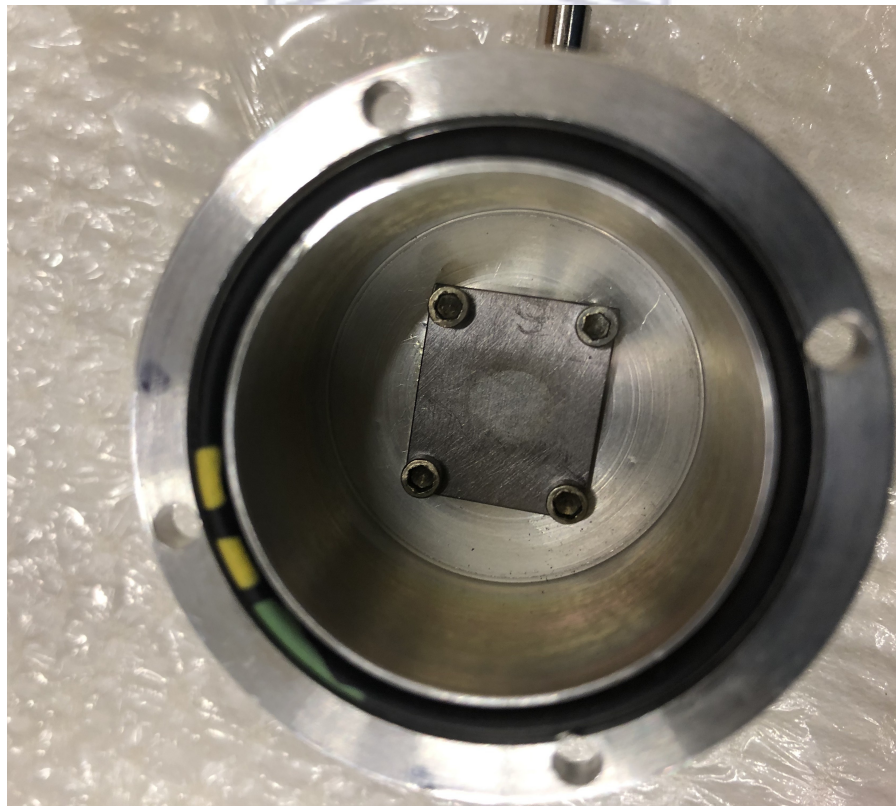
Figure 3.3: Target holder with the implanted target.

36
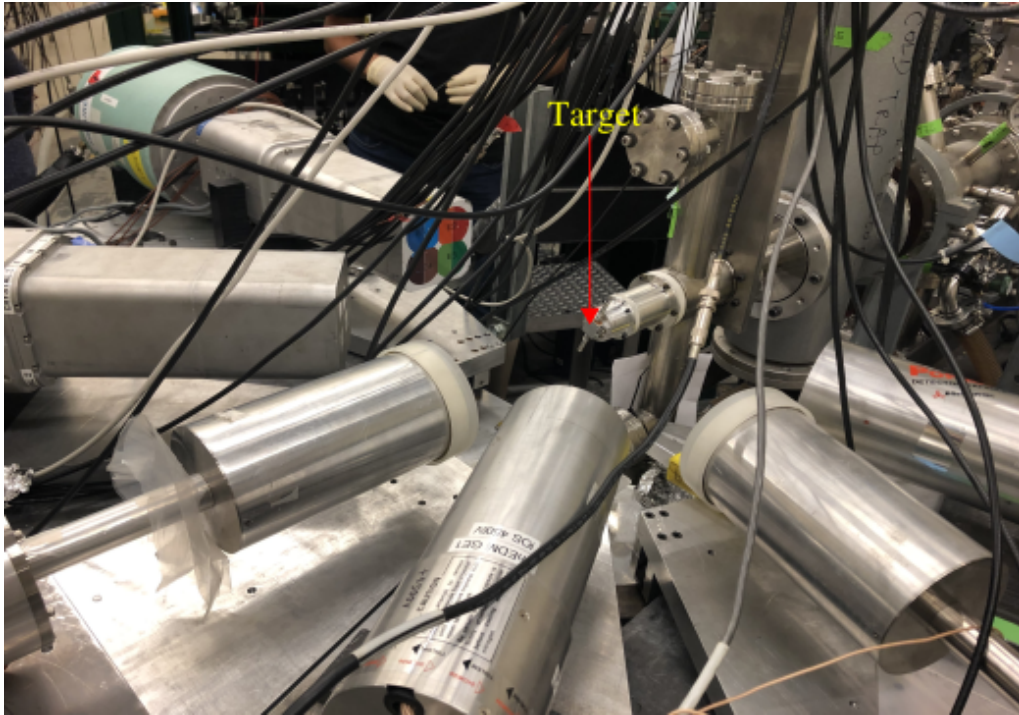
Figure 3.4: Photograph of the detector array, shown relative to the target position.
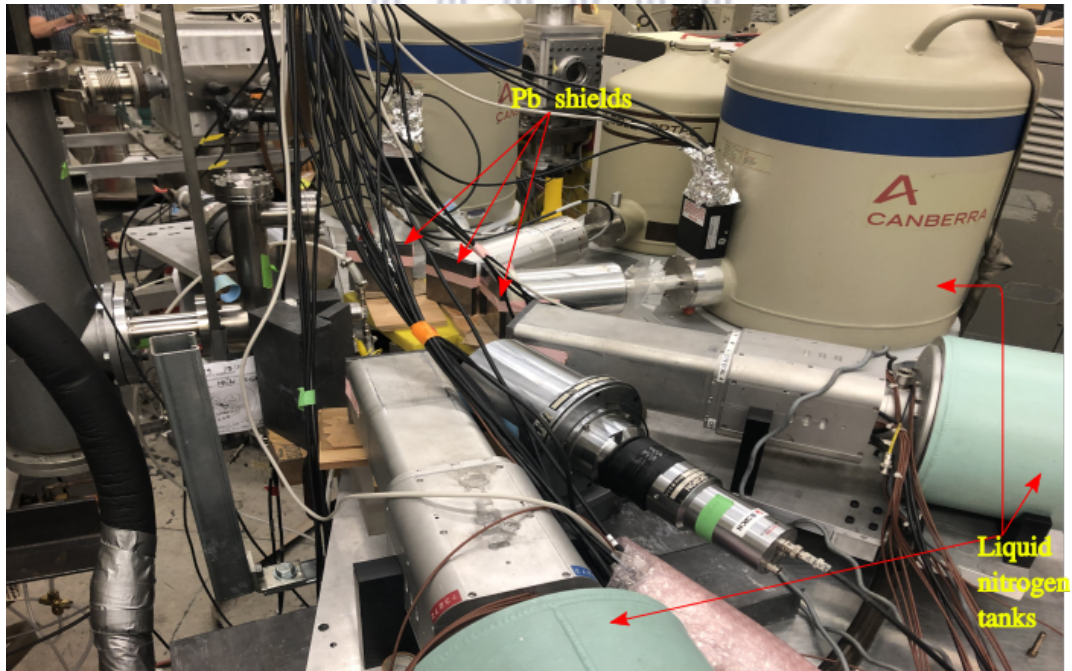
Figure 3.5: Picture of the detector array taken from another angle.
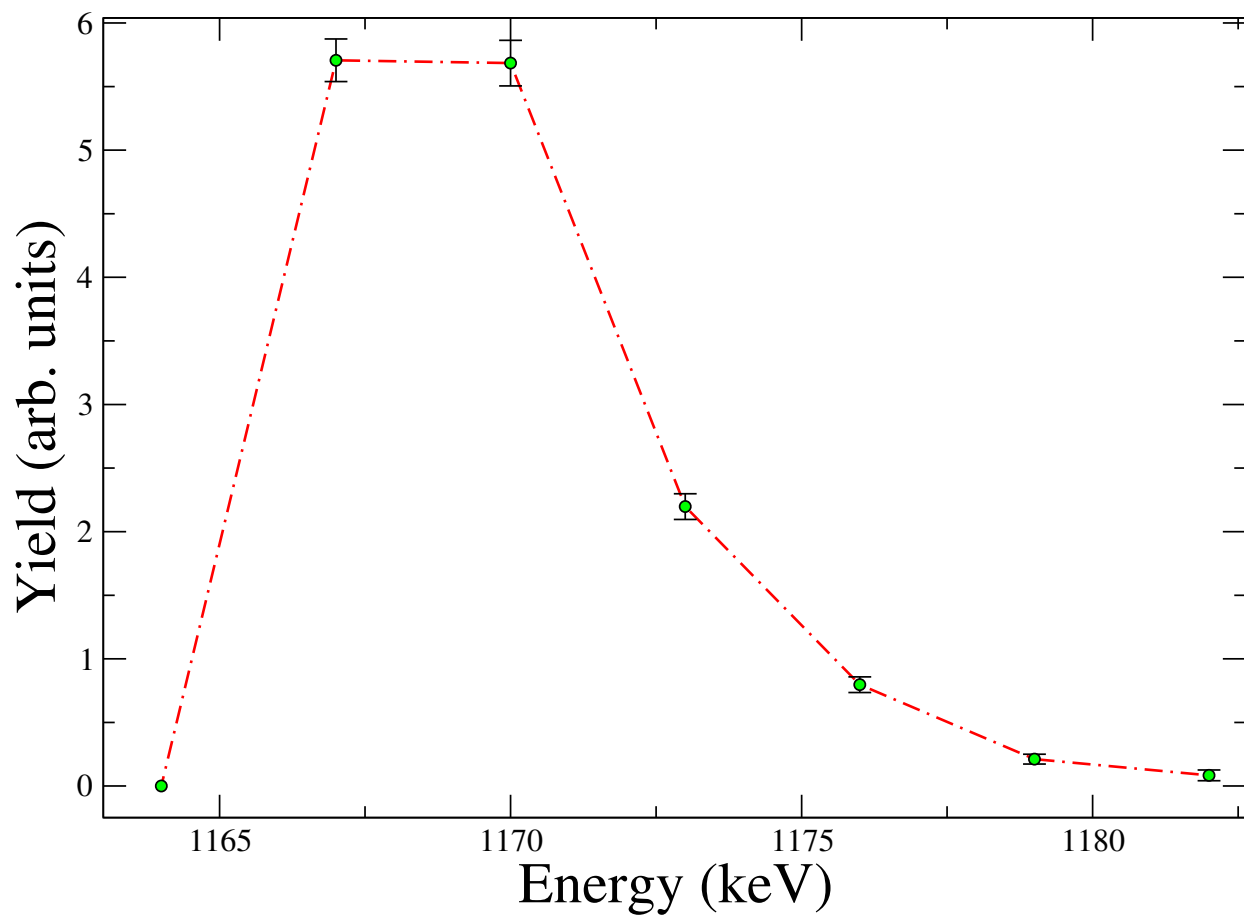
Figure 3.6: γ-ray yield curve as a function of the proton beam energy for 100% Canberra 2.

Detector	Detector angle with respect to the beam axis	Detector distance from target (cm)
80% ORTEC	0°	20
100% Canberra 1	-55°	21
100% Canberra 2	31.5°	21
Clover 1	62.5°	23
Clover 2	90°	23

Table 3.1: Detector geometry used for this experiment.

38

Chapter 4

Data Analysis and results

4.1 Gain drift corrections

Although the electronic modules for data acquisition were placed in a temperature controlled rack, amplifier gain variations needed to be taken into account prior to data analysis. Since the data were acquired event-by-event, the gain drift for each amplifier and ADC combination was monitored by dividing each experimental run into smaller subsets and registering the centroids for a few high statistics γ-ray peaks for each detector crystal over time. Each subsequent 'sub-run' was then gain-matched to the first 'sub-run' using a linear regression routine

$$x'_i = a_i + b_i x_i, \tag{4.1}$$

where the x'_i label the peak centroids of the first subset of the data and a_i, b_i are the gain correction coefficients for each 'sub-run'. We next implemented these parameters into the sorting code to perform gain-shift corrections using the formula

$$Ch'_i = a_i + b_i[Ch_i + (R - 0.5)], \tag{4.2}$$

where Ch_i is an integer number that represents an ADC event associated with γ-ray energy, R is a uniformly distributed random number between 0 and 1 and Ch'_i is the gain-drift corrected value, rounded off to the nearest integer.

A sample gain-corrected ^{56}Co γ-ray peak is shown in Fig. 4.1. All peaks in our data were fitted using a lineshape function that is the convolution of a Gaussian with a low-energy exponential tail [42], together
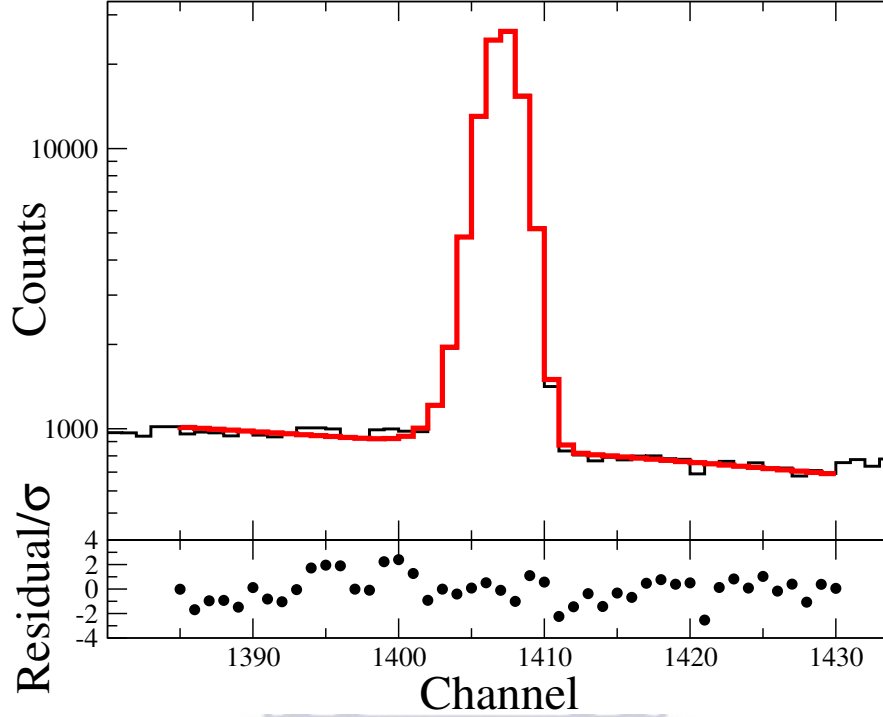
39

Figure 4.1: Sample fit to a 1238 keV γ-ray calibration peak from ^{56}Co.

with a smoothed step function that takes into consideration multiple Compton scattering. The fit function also incorporated a background component that could either be flat, linear or quadratic in nature. The example in Fig. 4.1 uses a linear background.

4.2 Energy calibration

The ^{56}Co source was made on-site via the ^{56}Fe(p, n) reaction and used to calibrate the HPGe detectors. The source emits well-characterized γ rays in the range of 846 keV $\leq E_\gamma \leq$ 3451 keV. A calibrated ^{56}Co γ-ray spectrum from one of the 100%-efficient Canberra detectors is shown in Fig 4.2. A ^{60}Co source was also used for calibration purposes and to perform important cross checks. As described below, the ^{60}Co source was not necessary for the final measurement of the mixing ratio. The energy calibration of each detector was performed using a linear regression

$$E_\gamma(i) = a + b\mu(i), \tag{4.3}$$

where the $\mu(i)$ are peak centroids obtained from fits such as the one shown in Fig. 4.1. The offset and gain coefficients a and b were then used to identify relevant peaks in the ^{20}Ne(p, γ) spectra. For the clover detectors, we sorted the data to obtain spectra from individual crystals, as well as in add-back mode, which involved adding the energies deposited in all four crystals of each clover. The add-back mode had

higher efficiency than the one obtained from adding individual crystals because of the counts recovered from Compton scattered events. The add-back energy calibration was such that

$$E_\gamma^{add}(i) = \sum_{j=4}^{4} \{[Ch_i'(j)]a_j + b_j\},\tag{4.4}$$

where $Ch_i'(j)$ is the gain-drift-corrected energy ADC value for that particular clover detector. The energy calibration coefficients for each detector crystal are listed in Table 4.1
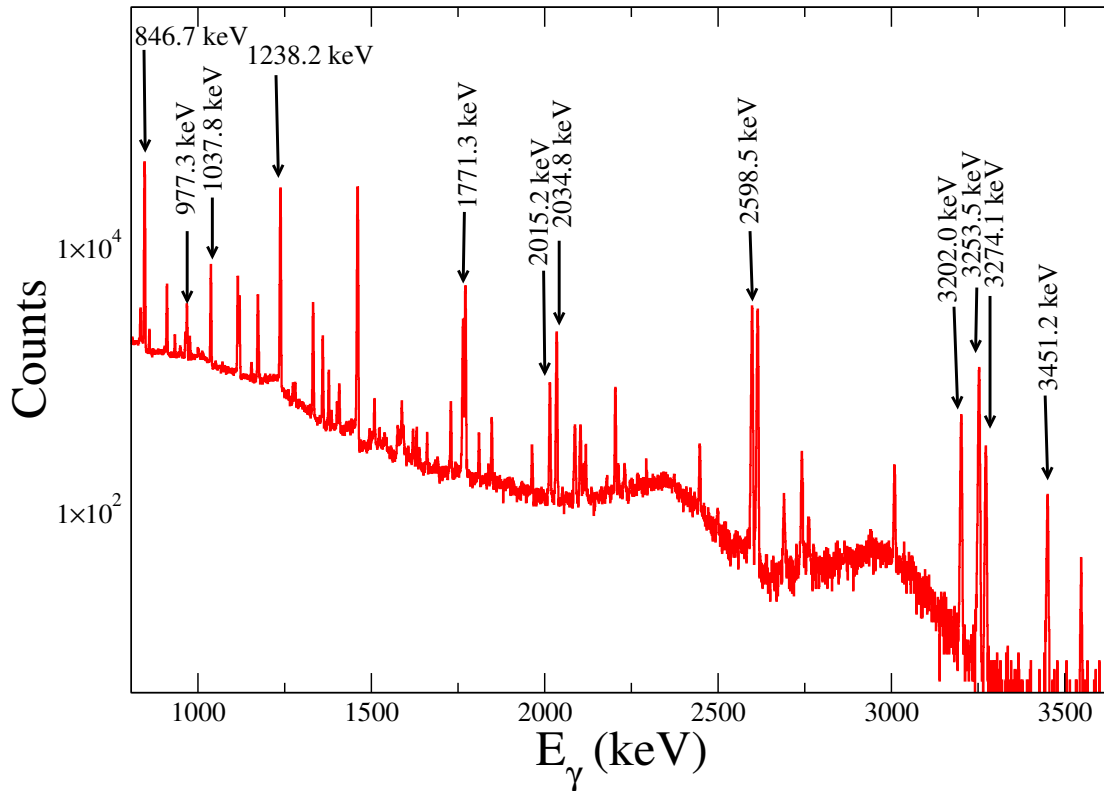
Figure 4.2: Energy calibrated ^{56}Co γ-ray spectrum from one of the 100%-efficient Canberra detectors. The most prominent peaks are labeled.

41
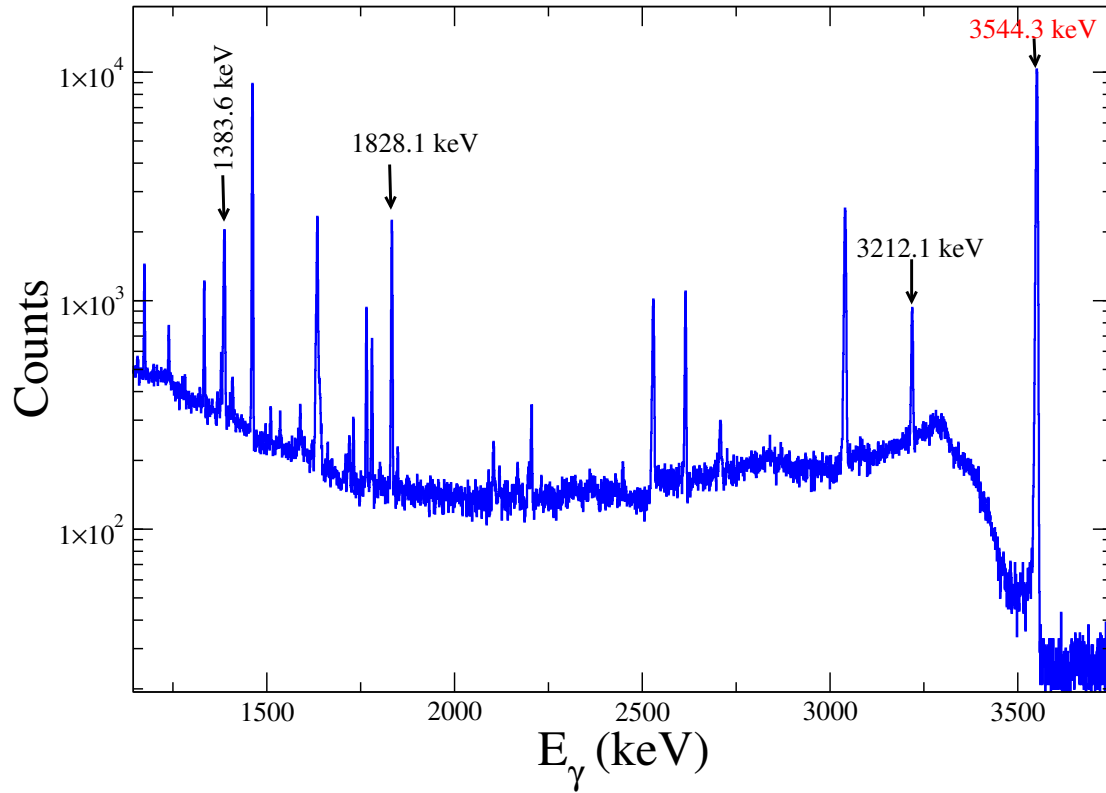
Figure 4.3: Calibrated ^{20}Ne(p,γ) spectrum obtained with a 100%-efficient Canberra detector. Some important γ-ray peaks from transitions within ^{21}Na are labeled.

Detectors	a	b
100% Canberra1	-65.97	0.88638
80% ORTEC 1	3.6	0.88719
100% Canberra 2	3.3	0.87728
C1E1	2.6	0.88964
C1E2	2.1	0.88756
C1E3	-1.1	0.89291
C1E4	-0.27	0.89083
C2E1	-1.5	0.89835
C2E2	-0.36	0.8910
C2E3	0.88	0.89679
C2E4	-1.5	0.89763

Table 4.1: Energy calibration coefficients for the HPGe detectors. Here the $CiEj$ label the clover crystals.

42

4.3　Relative efficiency calibration

Since the ^{56}Co source emits γ rays with well known intensities, it was used to determine the relative efficiency curve for each detector. This efficiency calibration was used to determine the unknown relative efficiency of the 3544 keV γ ray of interest. The relative efficiency for each ^{56}Co γ ray was determined using the simple formula

$$\epsilon_\gamma^{\text{rel}}(i) = \frac{N_\gamma(i)}{I_\gamma(i)}, \tag{4.5}$$

where $N_\gamma(i)$ is the area under a given peak and $I_\gamma(i)$ is its intensity, obtained from the National Nuclear Data Center (NNDC) database [39]. The ^{56}Co γ rays used for the efficiency calibration as well as their associated intensities are listed in Table. 4.2. Since the efficiency of γ-ray detection is energy-dependent and drops at both low and high energies, the relative efficiency curve was obtained from a polynomial fit to the ^{56}Co data, described by

$$\ln \epsilon_\gamma^{\text{fit}}(i) = \sum_{k=0}^{3} a_k \left[\ln E_\gamma(i)\right]^k. \tag{4.6}$$

This polynomial fit incorporated a χ^2-minimization procedure (with respect to each coefficient a_k), where

$$\chi^2 = \sum_{i=1}^{N} \frac{1}{\sigma_i^2} \left[\ln \epsilon_\gamma^{\text{rel}}(i) - \ln \epsilon_\gamma^{\text{fit}}(i)\right]^2, \tag{4.7}$$

with N being the number of data points and σ_i being the uncertainty in each $\epsilon_\gamma^{\text{rel}}(i)$.

The χ^2-minimization was performed by solving the resulting linear equations using the Gauss-Jordan elimination method [43]. The relative efficiency curves for each detector are shown in Figs 4.4. These efficiency curves were extrapolated to determine the efficiency of each detector at around 3544 keV. Since each detector would observe a Doppler-shifted energy for this γ-ray, it was important to cross-check the effects of the extrapolation in the efficiency curves. The Doppler-shifted γ-ray energy for each detector is

$$E_\gamma' = E_\gamma \left(1 + \frac{v}{c} \cos \theta_\gamma\right). \tag{4.8}$$

This can be determined from the $\left(\frac{v}{c}\right)$ for the recoiling compound ^{21}Na nucleus, which is $\approx 2 \times 10^{-3}$. For completeness the Doppler-shifted energies are listed in Table 4.3. The extrapolated relative efficiencies at

Energy	Intensity
(keV)	(%)
1037.843(4)	14.05(4)
1771.357(4)	15.41(6)
2015.215(5)	3.016(12)
2034.791(5)	7.77(3)
2598.5(4)	16.97(4)
3202.029(8)	3.209(12)
3253.503(4)	7.923(21)
3273.079(4)	1.8759(2)
3451.232(4)	0.949(5)

Table 4.2: ^{56}Co γ rays used for the efficiency calibration. The energy and intensity values are from Ref. [39].

these energies are represented by squared-shaped points as shown in Fig. 4.4. The maximum shift, which was expected for the $\theta_\gamma = 0°$ detector, was found to be ≈ 8.5 keV.

44
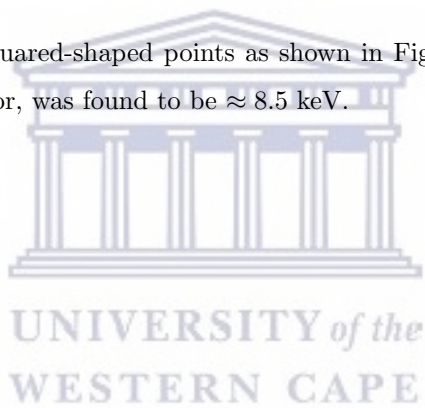
Figure 4.4: Continued

Figure 4.4: Polynomial fits to experimental relative efficiencies for each detector.

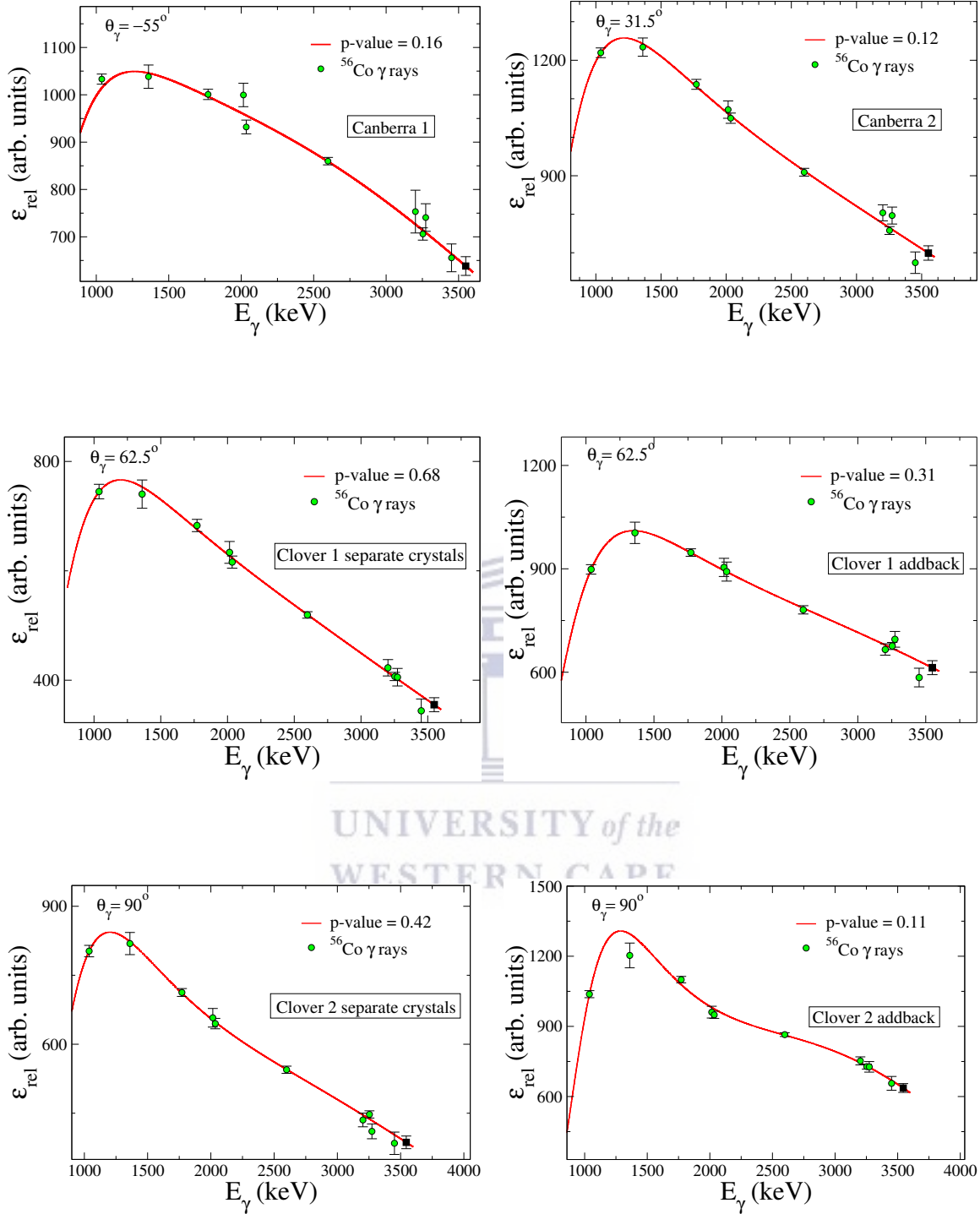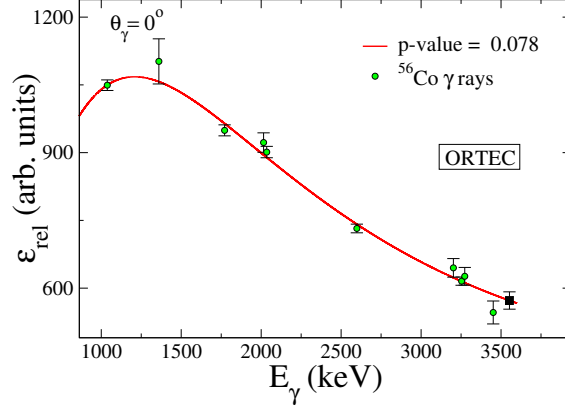| Detector	θ_γ	E'_γ	$E'_\gamma - E_\gamma$
	(deg)	(keV)	(keV)
ORTEC	0	3552.8	8.5
Canberra 1	-55	3549.2	4.9
Canberra 2	31.5	3551.5	7.2
Clover 1	62.5	3548.2	3.9
Clover 2	90	3544.3	0.0

Table 4.3: Doppler-shifted energy for the 3544.3 keV γ ray in each detector.

4.3.1 PENELOPE Monte Carlo simulations.

It may be noted that the 3544 keV γ ray is around 93 keV higher than the highest energy calibration γ-ray peak from ^{56}Co (this is the 3451 keV peak, which had sufficient statistics). This extrapolation increases to beyond 100 keV for the 0° detector that observes maximal Doppler shift. Keeping this in mind, we performed Monte Carlo simulations to estimate each detector's efficiency and to have a better understanding of associated systematic effects. The simulations were performed using the Penetration and ENErgy LOss of positrons and Electrons (PENELOPE) radiation transport code [44]. The experimental set up constructed within the PENELOPE package is shown in Fig. 4.5.

The first set of simulations were used to estimate the relative efficiencies of each γ ray in Table. 4.2, assuming an isotropic distribution of photons. The random directions for the photons were determined in the simulations from the probability of emission within a unit sphere, described by

$$p(\theta, \phi)d\theta d\phi = \frac{1}{4\pi} \sin\theta d\theta d\phi = \left[\frac{\sin\theta}{2}d\theta\right]\left[\frac{1}{2\pi}d\phi\right].$$
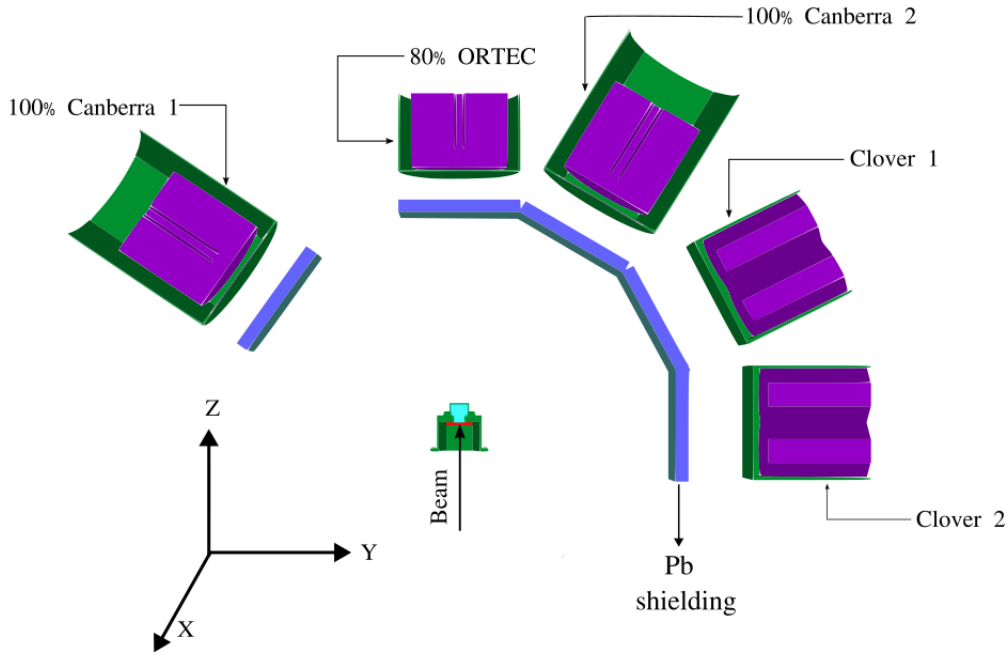(4.9)

46

Figure 4.5: A schematic display of the target-detector setup used for the Monte Carlo simulations. As mentioned previously, the Pb shielding is present to minimize the effects of γ-ray summing.

In the above, θ and ϕ are independent random variables with probability density functions (PDFs)

$$p_\theta = \frac{\sin\theta}{2} \quad \text{and} \quad p_\phi = \frac{1}{2\pi}. \tag{4.10}$$

The transformation method [45] was used to generate a set of random numbers that follow these PDFs. This is obtained from the corresponding cumulative distribution functions (CDFs)

$$C_\theta = \int_0^\theta \frac{\sin\theta'}{2}d\theta' \quad \text{and} \quad C_\phi = \int_0^\phi \frac{1}{2\pi}d\phi', \tag{4.11}$$

where $C = \int_a^b p(x)dx$ within $[a,b]$. The above easily simplify to

$$C_\theta = \frac{1 - \cos\theta}{2} \quad \text{and} \quad C_\phi = \frac{\phi}{2\pi}. \tag{4.12}$$

Since the range of the CDF is $[0,1]$, these can be generated using uniformly distributed random numbers between 0 and 1. In such a scenario, isotropic showers of photons are produced using the random polar variables,

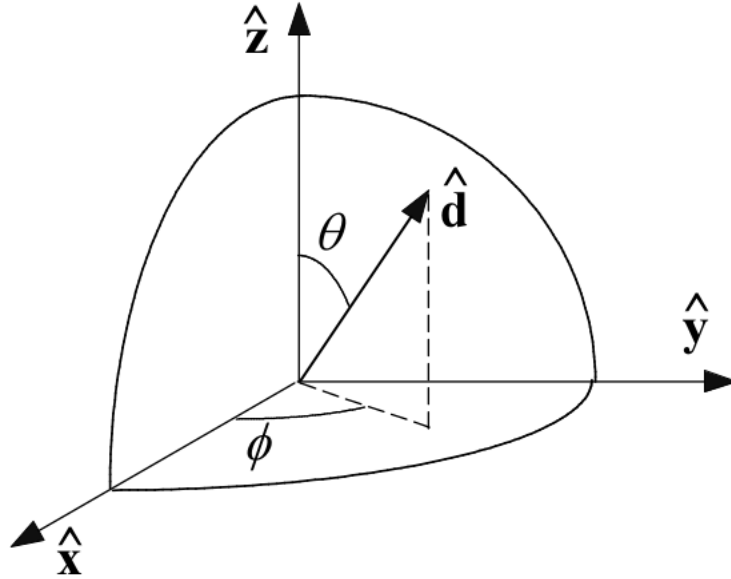$$\theta = \arccos(1 - 2U) \quad \text{and} \quad \phi = 2\pi V, \tag{4.13}$$

47

Figure 4.6: Coordinate system used for the simulations. Here θ and ϕ are the polar and azimuthal angles of the unit vector $\hat{d}$. The direction of the beam and the quantization axis is defined by $\hat{z}$.

where U and V are uniform random deviates in the range $[0, 1]$ [46]. The coordinate system used for the simulations is shown in Fig. 4.6.

This method of generating an isotropic distribution was implemented within PENELOPE and the absolute γ detection efficiency for each detector was determined using 5×10^6 photons emitted at each γ-ray energy in Table. 4.2. The simulated efficiencies were then overlaid and normalized to experimentally determined values. Figure 4.7 shows one such comparison for the $0°$ detector, which required maximal shifting for the extrapolation to 3544 keV. While the simulation results yield higher efficiencies at lower energies (which is not unexpected considering additional low-energy absorptions not included in the simulations), the overall agreement between the two data sets is reasonable. The extrapolated efficiency at 3544 keV also shows excellent agreement with the simulated value. This conveys that the extrapolations are not far off the true value.

4.4 Determination of γ-ray yields and mixing ratio

The relative 3544 keV γ-ray yield for each detector was determined from its peak area and the extrapolated relative efficiency using the expression

$$\text{Yield} = \frac{\text{Area (3544 keV)}}{\epsilon_\gamma^{\text{rel}}(3544 \text{ keV})}.$$

(4.14)

48
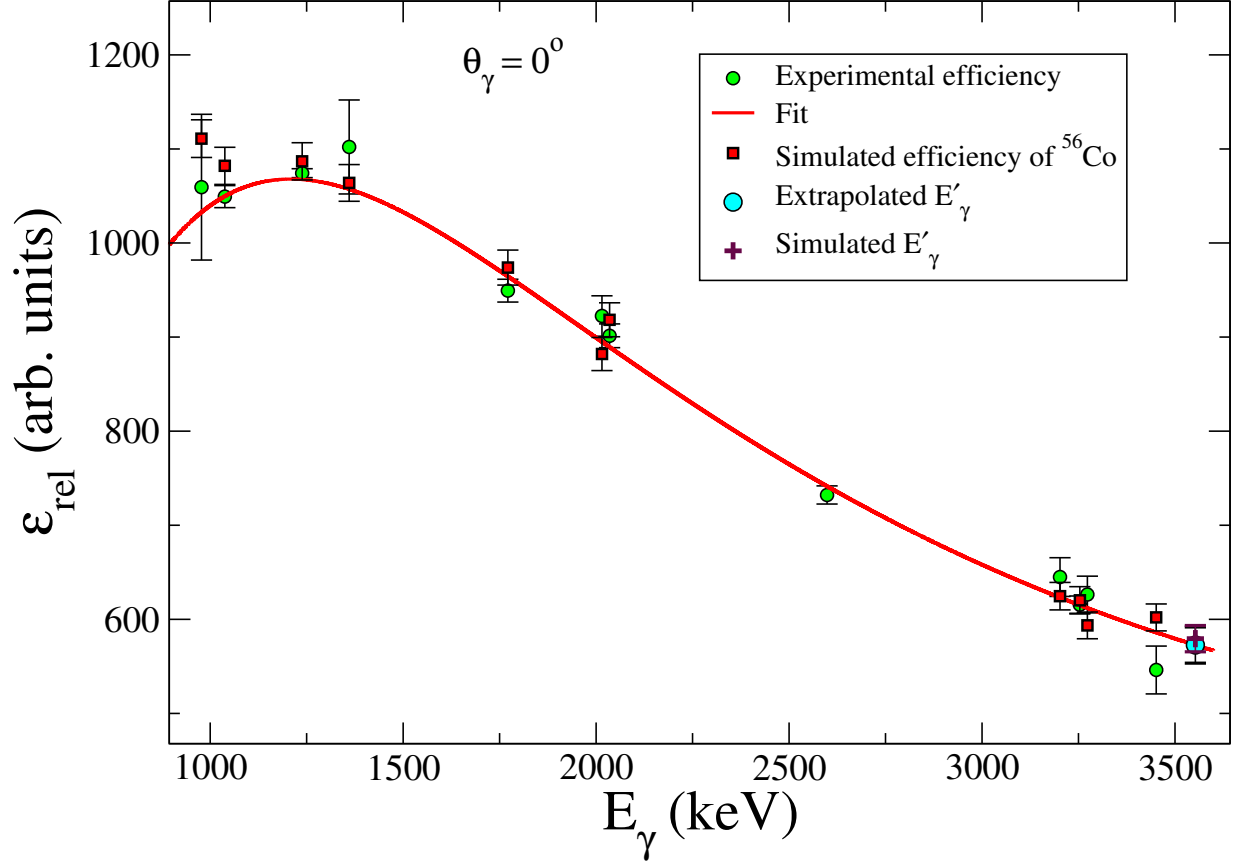
Figure 4.7: Sample plot of experimental and simulated efficiencies for the ORTEC detector.

The fits to the 3544 keV peak for each detector and the measured yields are plotted in Figs. 4.4 and 4.9. The measured yields in Fig. 4.9 were next fit with a polynomial function that describes the angular distribution

$$W(\theta) = a_0 + a_2 P_2(\cos\theta) + a_4 P_4(\cos\theta), \tag{4.15}$$

where θ is the polar angle in Fig. 4.6. As previously explained with Eq. 2.98 in Chapter 2, the $E2/M1$ mixing ratio δ is embedded in the above experimental a_k coefficients. However, to determine the mixing ratio one needs to take into account the finite solid angle subtended by the detectors. Additionally, the alignment coefficients for the initial state that emits the γ ray also need to be known. Under normal circumstances, when identical coaxial detectors are used to take measurements at different angles, the angular distribution is expressed as

$$W(\theta) = \sum_{K=\text{even}} Q_K A_K P_K(\cos\theta), \tag{4.16}$$

where Q_K are attenuation coefficients described by [35]

49
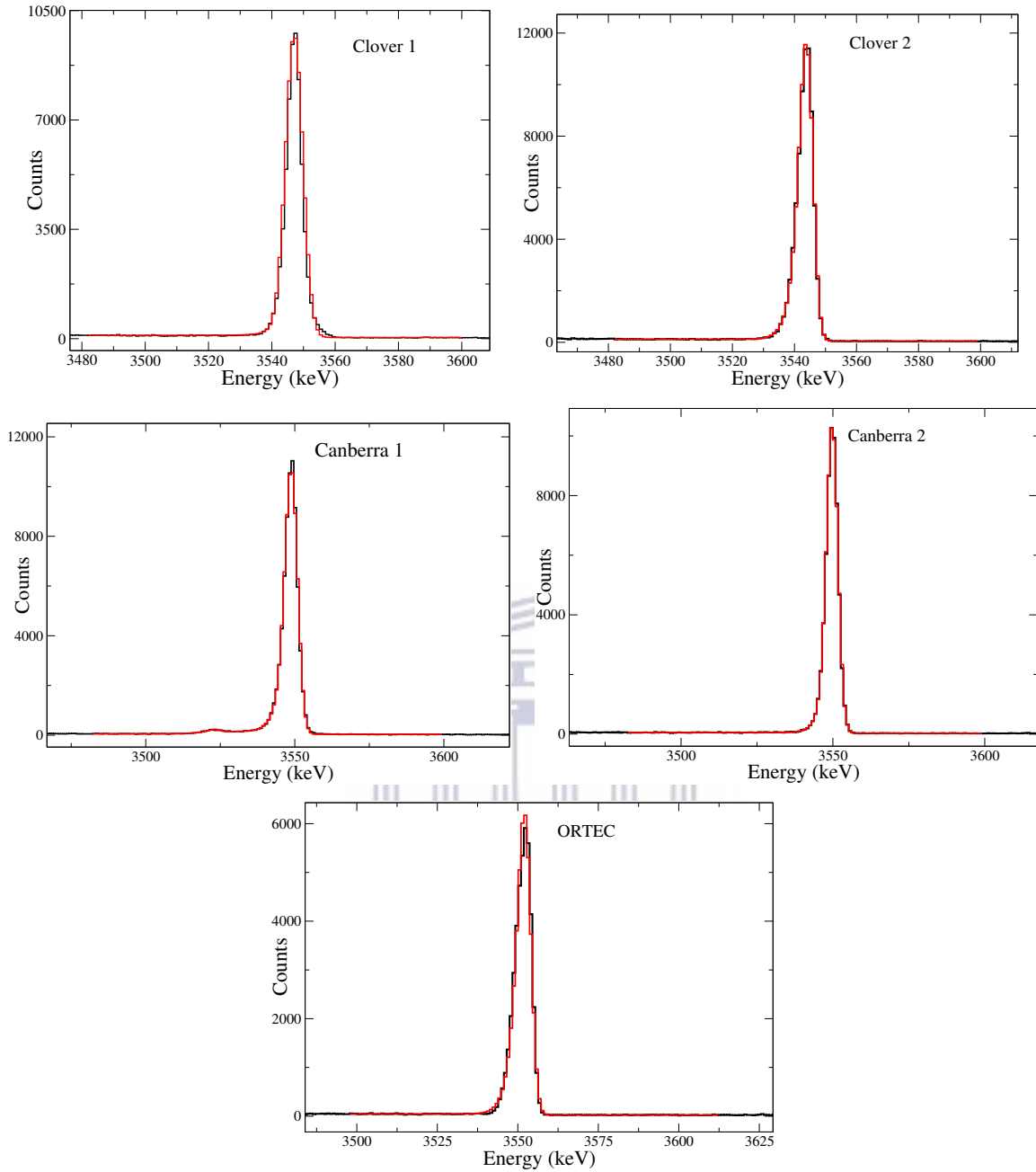
Figure 4.8: Fits to the 3544 keV γ-ray peak in the ^{20}Na(p,γ) spectrum for each detector.

$$Q_K = \frac{\int_0^{\beta_{\max}} P_K\left(cos\beta\right)\eta(\beta, E)\sin\beta d\beta}{\int_0^{\beta_{\max}} \eta(\beta, E)\sin\beta d\beta}. \tag{4.17}$$

In the above, β is the angle between the location where the γ ray strikes a detector and the detector's symmetry axis, and $\eta(\beta, E)$ represents the photo-peak efficiency of a γ ray with energy E. The theoretical

50

A_K coefficients for a $J_1 \to J_2$ transition are

$$A_K = \frac{1}{1 + \delta^2} \left[f_K(LLJ_1J_2) + 2\delta f_K(LL'J_1J_2) + \delta^2 f_K(L'L'J_1J_2) \right],$$ (4.18)

where $f_K(LL'J_1J_2) = B_K(J_1)R_K(LL'J_1J_2)$. The B_K (alignment) and R_K (angular momentum) coefficients have been already defined in Chapter 2.
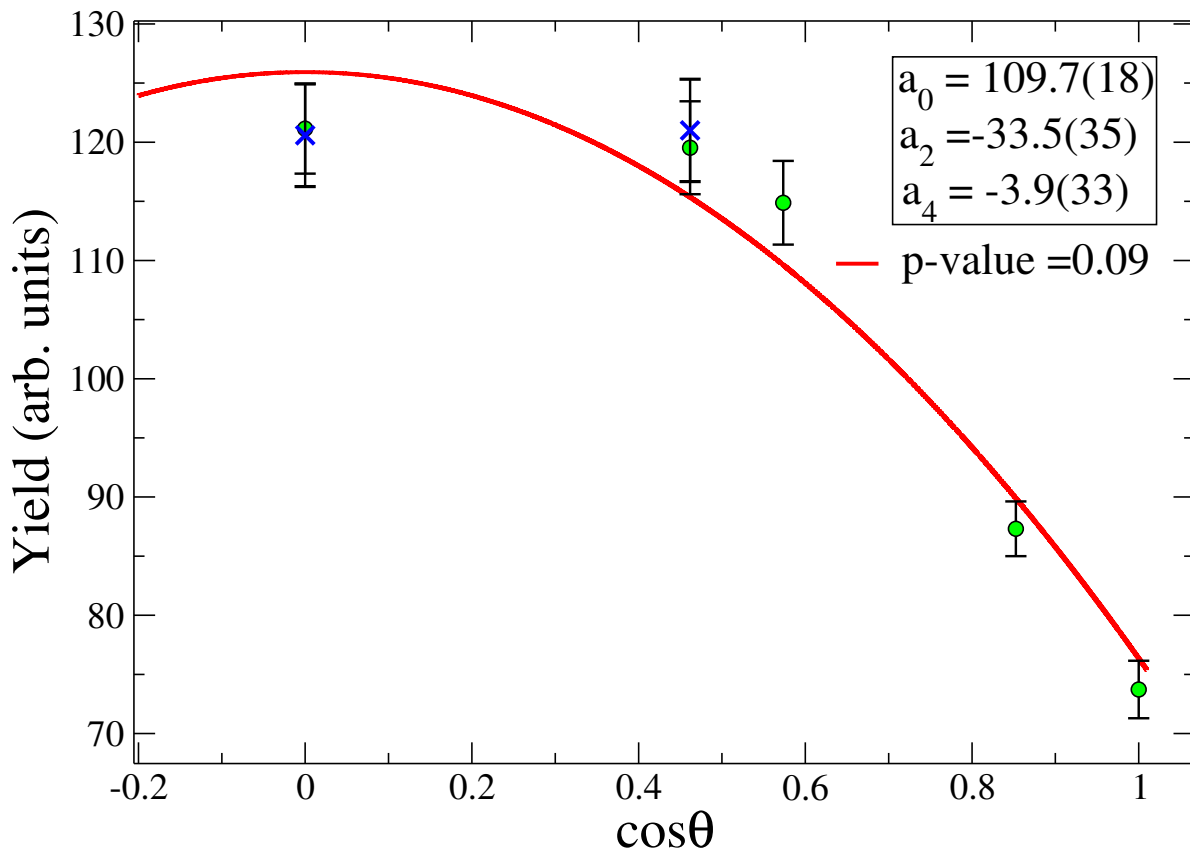
Figure 4.9: Measured yields for the 3544 keV γ-ray. The data obtained from a separate crystal analysis of the clovers are represented by **x**. These are overlaid with the yields obtained from the add-back spectra for comparison.

4.4.1 Simulations to correct for the finite solid angle effect

The form of Eq. 4.17 is not applicable here as the detectors used for this experiment were not identical. Therefore a Monte Carlo approach had to be used to determine the solid-angle correction coefficients Q_K. The Monte Carlo prescription was to use known values of A_2^{inp} and A_4^{inp} to generate anisotropically 3544 keV γ-ray photons, assuming the experimental geometry in Fig. 4.5. The assumed anisotropic angular distribution

51

Detector	$Y(i)$
ORTEC	73.9(26)
Canberra 1	115.3(36)
Canberra 2	87.5(23)
Clover 1	121.0(43)
Clover 2	120.6(43)

Table 4.4: Yield for each detector at Doppler-shifted energies.

in the simulations was of the form

$$f(\theta) = 1 + A_2^{\text{inp}} P_2(\cos\theta) + A_4^{\text{inp}} P_4(\cos\theta). \tag{4.19}$$

Then the Q_K values could be determined from the simulated yields, given the angular distribution in Eq. 4.19, using the ratio

$$Q_K = \frac{A_K^{\text{obs}}}{A_K^{\text{inp}}}. \tag{4.20}$$

For this part the angular distribution was generated within PENELOPE using Von Neumann's rejection-acceptance method. This method requires the generation of two uniform random variables v and x_0, under the conditions that

- if $v \leq f(x_0)$, then the points are accepted

- if $v > f(x_0)$, then both v and x_0 are rejected and a new pair of random numbers is generated.

In the above $x_0 \in [-1, 1]$ and $v \in [0, 2]$, so that Eq. 4.19 is satisfied. Both these random deviates were generated similarly as in Eq. 4.13. Simulated results for a test case with randomly chosen values for $A_2^{\text{inp}} = 0.224$ and $A_4^{\text{inp}} = 0.653$ are shown in Fig. 4.10.

Afterwards, we generated 80×10^6 showers of the 3544 keV γ ray for different values of A_K^{inp} {0.5, 0.7 and 0.9}. The number of accepted events was also recorded in our simulations. These showed that approximately 50% of the initial showers were rejected in the simulations. The observed yield for each detector was determined by

$$Y_{\text{obs}} = \left(\frac{N_{\text{d}}}{N_{\text{a}}}\right), \tag{4.21}$$

where N_{a} is the number of counts accepted and N_{d} is the counts detected.

As an additional test to check the reliability of our simulation framework, we generated an isotropic distribution of 40×10^6 3544 keV γ rays, using the transformation method mentioned earlier. Here the absolute
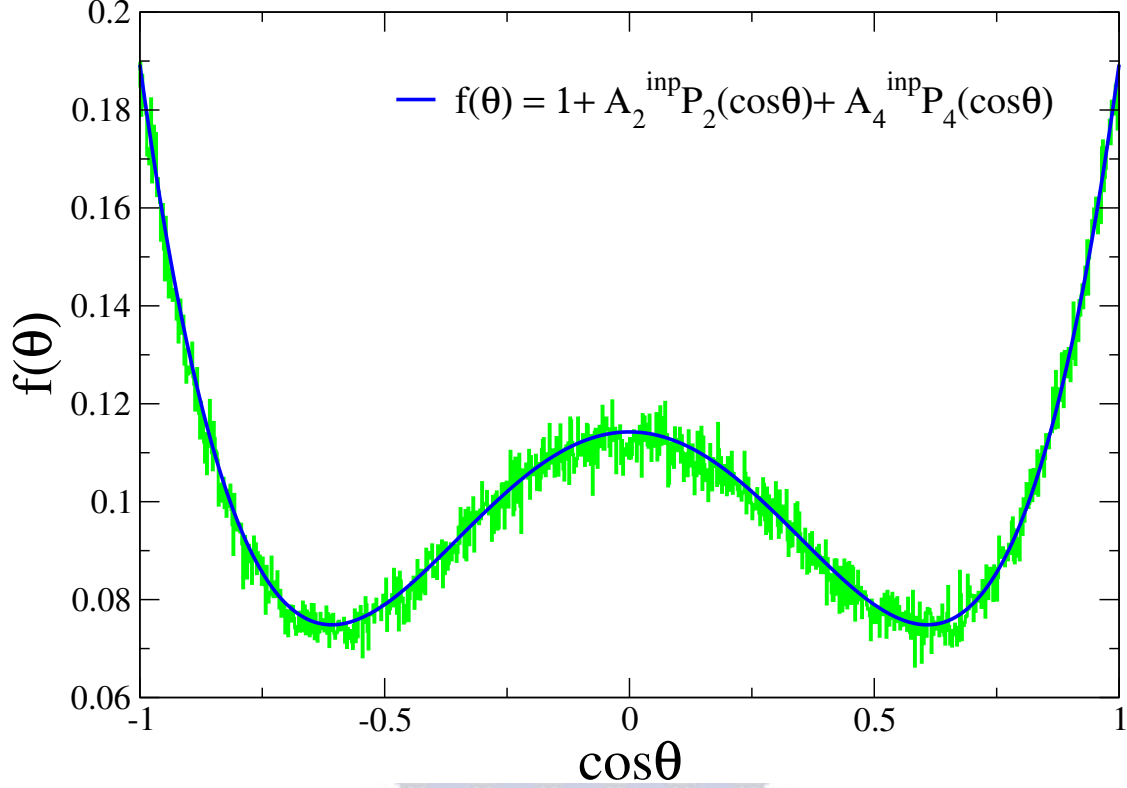
Figure 4.10: Histrogram of a simulated angular distribution using the rejection-acceptance method, with $A_2^{\text{inp}} = 0.224$ and $A_4^{\text{inp}} = 0.653$. The analytical function is overlaid as a solid line for comparison.

efficiency of each detector was obtained from the ratio

$$\epsilon_{\text{abs}} = \frac{N_{\text{d}}}{N_{\text{s}}}, \tag{4.22}$$

where N_{s} is the number of γ rays emitted at the source location isotropically. If the simulation model and methods used were correct, then the ratio $\frac{Y_{\text{obs}}}{\epsilon_{\text{abs}}}$ for each data point would agree with the analytical value of $f(\theta)$ at that point. An example result for one such comparison, with $A_2^{\text{inp}} = 0.5$ and $A_4^{\text{inp}} = 0.5$ is displayed in Fig. 4.11. This figure shows excellent agreement between $\frac{Y_{\text{obs}}}{\epsilon_{\text{abs}}}$ and the theoretical distribution $f(\theta)$ at each data point. This alludes that our simulation framework being well founded.

Once the above was confirmed the simulation results were used to determine the Q_{K} coefficients. However, it was important to separate the solid angle contribution from the (energy-dependent) intrinsic detection efficiency for each detector.

For an isotropic source, the absolute and intrinsic efficiencies are related through

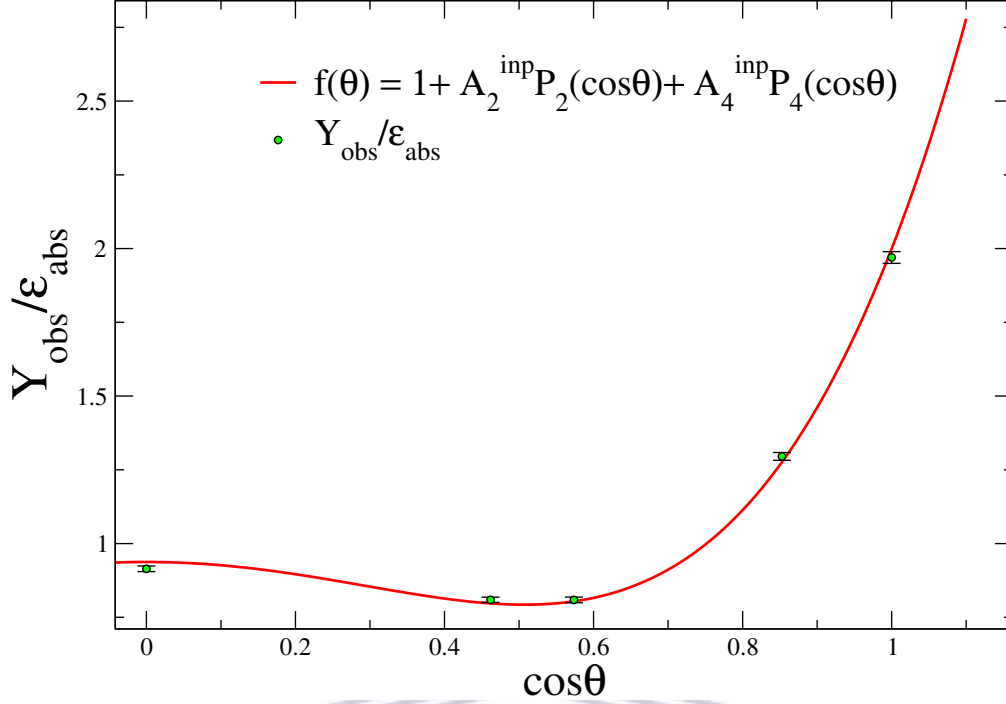$$\epsilon_{\text{abs}} = \epsilon_{\text{int}} \left(\frac{\Omega}{4\pi} \right), \tag{4.23}$$

53

Figure 4.11: Simulated ratio of the yields to absolute efficiencies for $A_2^{\text{inp}} = 0.5$ and $A_4^{\text{inp}} = 0.5$.

where Ω is the solid angle subtended by each detector. For a point source at a distance d from a cylindrical detector, the solid angle is given by (see Fig. 4.12),

$$\Omega = 2\pi \left(1 - \frac{d}{\sqrt{d^2 - a^2}} \right). \tag{4.24}$$

Here d is the source-to-detector distance, a is the radius of the coaxial HPGe detector and A is the area of the face of the detector that is visible to the source as shown in Fig. 4.12. For $d \gg a$, the solid angle is estimated to be

$$\Omega \approx \frac{A}{d^2}. \tag{4.25}$$

Eq. 4.23 further simplifies to

$$\frac{\epsilon_{\text{abs}}}{\epsilon_{\text{int}}} \approx \frac{a^2}{4d^2}, \tag{4.26}$$

clearly shows that the solid angle contribution can be determined if both the absolute and intrinsic efficiencies are known for each detector.

The next step was to obtain the intrinsic efficiency (ϵ_{int}) for each detector. These could be determined from the simulations by focusing a cone of monoenergetic γ rays at 3544 keV towards the direction of each
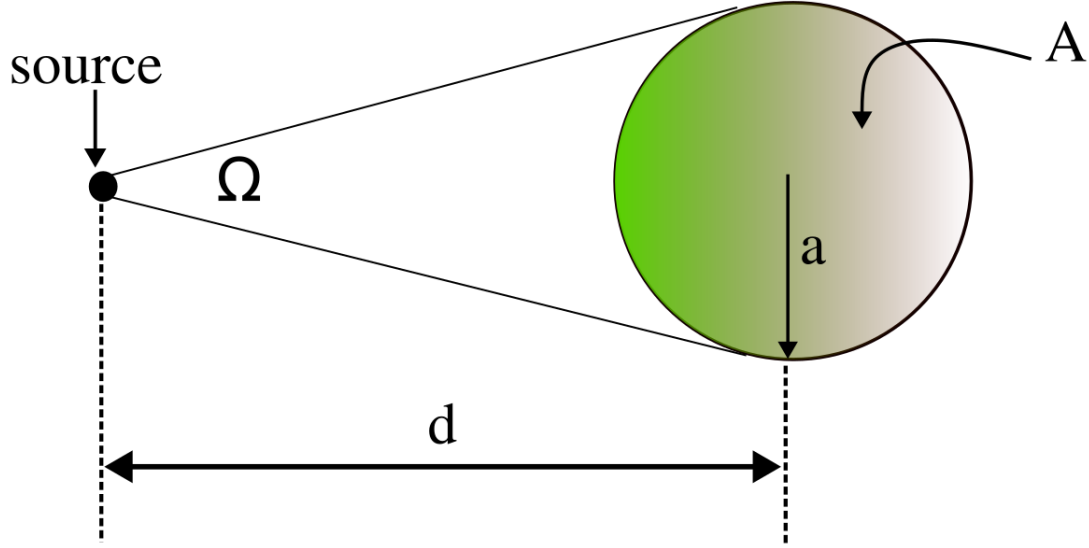
54

Figure 4.12: Geometric representation of the solid angle (Ω) subtended by a solid object.

detector from the target location (assuming that the clovers can be approximated to be nearly coaxial). The intrinsic efficiency for each HPGe detector can then be obtained using the ratio

$$\epsilon_{\text{int}} = \frac{N_{\text{d}}}{N_{\text{i}}},$$ (4.27)

where N_{i} is the number of γ rays incident on the detector and N_{d} is the number detected under the photopeak. For this part of the analysis 10^6 γ rays at $E_\gamma = 3544$ keV were generated for each detector.

For these simulations, performed for individual detectors located at different angles, the method was first developed for a cylindrically symmetric detector along the $\hat{z}$ axis ($\theta_\gamma = 0°$, along beam direction), as shown in Fig. 4.13.

As shown in Fig. 4.13, the maximum angle subtended by the detector is

$$\theta_{\text{max}} = \arctan\left(\frac{a}{d}\right).$$ (4.28)

This information was used to generate a cone of photons so that it is always incident on the face of the detector using the randomization procedure

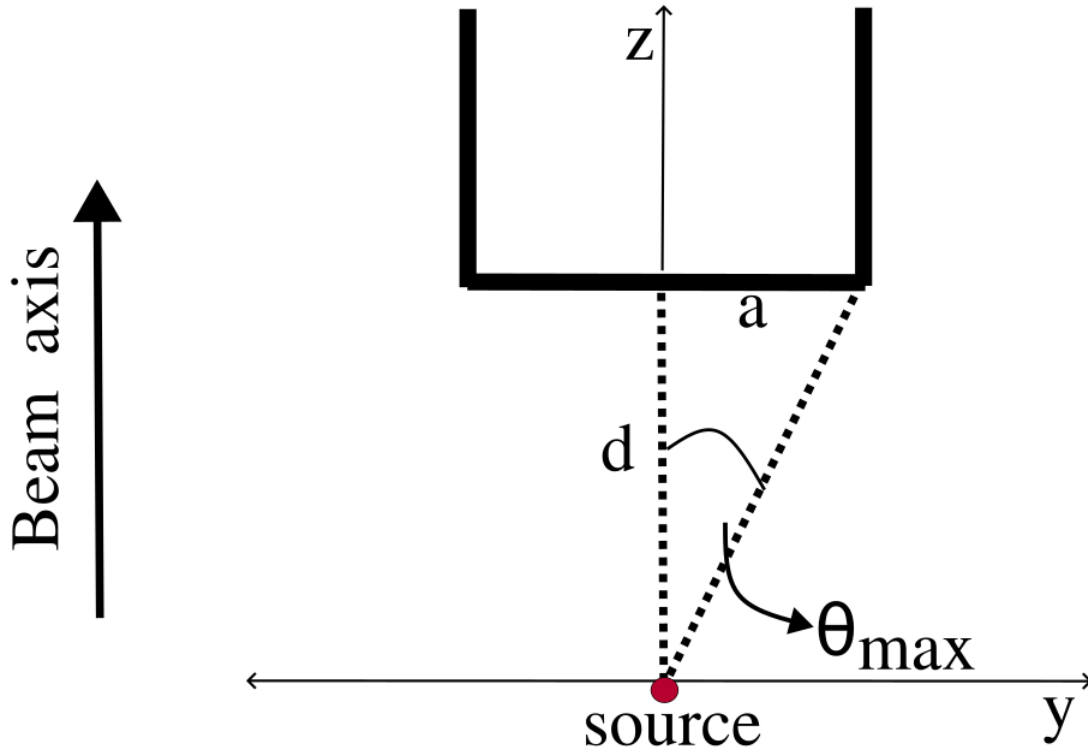$$\cos\theta = 1 - U[1 - \cos\theta_{\text{max}}]$$ (4.29)

55

Figure 4.13: Construction for the cone distribution, where d is the distance from the source to the detector's surface, a is the radius of the germanium crystal and $\theta_{\max}$ is the maximum angle subtended for a particular case shown here.

and

$$\phi = 2\pi V, \tag{4.30}$$

where U and V are uniform random numbers between $[0, 1]$. This was repeated for the other detectors using a rotation, as illustrated in Fig. 4.14. The basis vectors are $\hat{e}_y = (1, 0)$ and $\hat{e}_z = (0, 1)$. Therefore, for an arbitrary point $P(y, z)$ to be rotated about the $\hat{x}$-axis by an angle θ,

$$\mathbf{P^*} = R\mathbf{P},$$

where R is the rotation matrix

$$\begin{bmatrix} y* \\ z* \end{bmatrix} = \begin{bmatrix} \cos\theta & \sin\theta \\ -\sin\theta & \cos\theta \end{bmatrix} \begin{bmatrix} y \\ z \end{bmatrix}. \tag{4.31}$$

Once the ϵ_{int} values were obtained for each detector using this procedure, together with ϵ_{abs}, they were used to verify the solid angle subtended for each detector. A comparison between these results and calculated
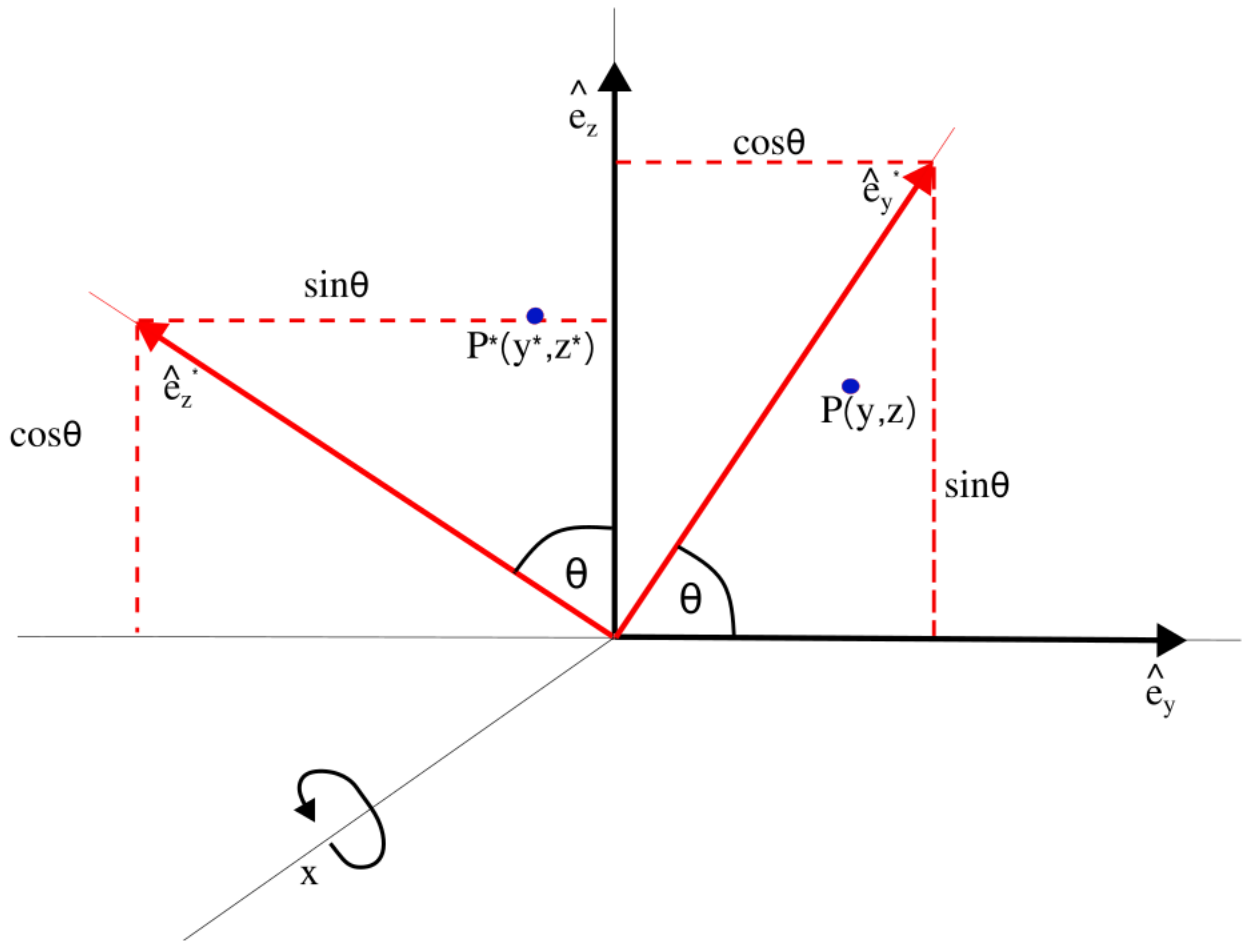
Figure 4.14: Rotation of the z and y axis by angle θ about the x-axis.

values is shown in Table. 4.5. The excellent agreement again verified that the simulations were correct.

Detector	$a^2/4d^2$	$\epsilon_{\text{abs}}/\epsilon_{\text{int}}$
Canberra 1	0.00767	0.00769
Canberra 2	0.00767	0.00733
ORTEC 1	0.00842	0.00861
Clover1	0.00800	0.00854
Clover 2	0.00800	0.00846

Table 4.5: Simulated solid angle corrections compared with analytical results.

These results were finally used to extract Q_K values using the simulated yields that were corrected for the intrinsic efficiency. This is shown in Fig. 4.15, for a test case that used data generated with $A_2^{\text{inp}} = 0.5$ and

Figure 4.15: Simulated ratio of the yields to the intrinsic detector's efficiency for A_K^{inp}=0.5 as a function of the detector's position.

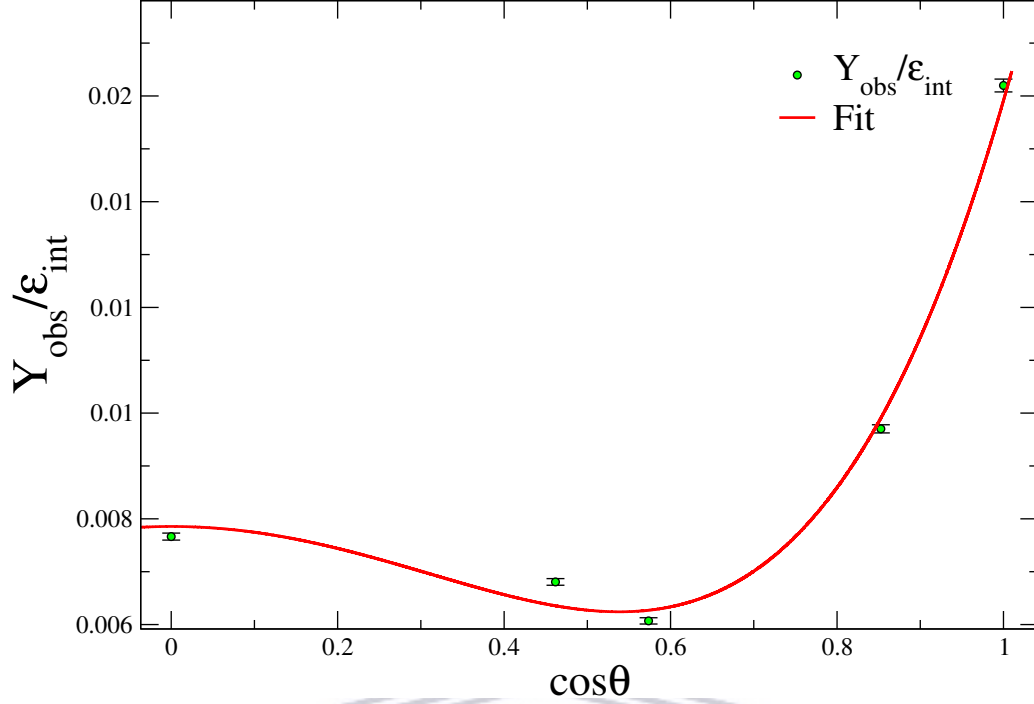| $A_2^{\text{inp}}=A_4^{\text{inp}}$	A_2'	A_4'	Q_2	Q_4
0.5	0.457	0.549	0.913	1.097
0.7	0.648	0.698	0.925	0.997
0.9	0.842	0.903	0.936	1.003

Table 4.6: Extracted Q_K values for given input A_K^{inp} in the simulations.

$A_4^{\text{inp}} = 0.5$. The simulated yields were fitted with a distribution of the form

$$W(\theta) = A_0 \left[1 + A_2' P_2 \left(\cos \theta \right) + A_4' P_4 \left(\cos \theta \right) \right], \tag{4.32}$$

where $A_K' = \frac{A_K}{A_0}$. The fit results for the A_K coefficients were then used to extract the Q_K values using,

$$Q_K = \frac{A_K'}{A_K^{\text{inp}}}. \tag{4.33}$$

The weighted mean of the Q_K values obtained from independent simulations (whose results are plotted in Fig. 4.16) are listed in Table 4.7.

Once the Q_K values were determined, the final step of the analysis involved obtaining the mixing ratio, δ.

58

	Q_2	Q_4
Add-back included	0.927	1.021

Table 4.7: Computed values of Q_2 and Q_4 from PENELOPE simulations.
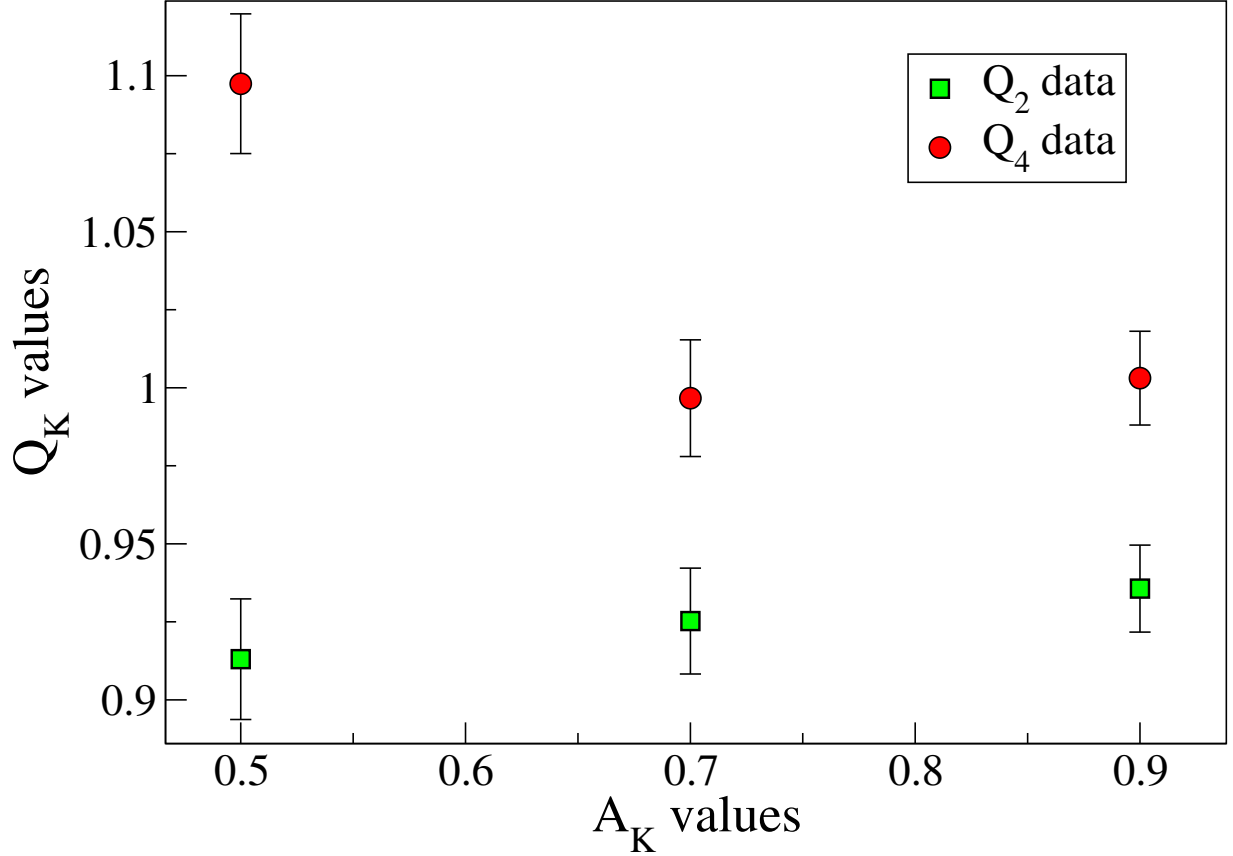
Figure 4.16: Deviation of the Q_K values for various cases of fixed A_2 and A_4 that consist of the add-back spectrum of the clovers.

Since the ^{20}Ne target nuclei have spin-parity $J^\pi = 0^+$ and the final state in ^{21}Na produced by the ^{20}Ne(p, γ) resonance has $J^\pi = \frac{5}{2}^+$, the orbital angular momentum ℓ carried by the protons for this particular resonance is $\ell = 2$. This yields alignment coefficients for the $\frac{5}{2}^+$ state to be $B_2(\frac{5}{2}) = -1.069$ and $B_4(\frac{5}{2}) = 0.9258$. The values of the R_K and f_K coefficients are shown in Table 4.8.

These values were used to calculate the angular distributions for arbitrary values of the mixing ratio δ,

K, L, L'	$R_K(LL'J_1J_2)$	$f_K(LL'J_1J_2)$
2, 1, 1	0.3742	-0.400
2, 1, 2	-0.9487	1.014
2, 2, 2	-0.1909	0.2041
4, 2, 2	0.7054	0.6531

Table 4.8: R_K and $f_K(LL'J_1J_2)$ values for the $\frac{5}{2}^+ \to \frac{3}{2}^+$ transition from the resonant state at 3544 keV.

incremented by small steps $\Delta\delta$. At each point, the χ^2 is defined by

$$\chi^2 = \sum_{i=1}^{N} \left[\frac{W_c(i) - W_m(i)}{\sigma_m(i)} \right]^2, \tag{4.34}$$

where N is the number of data points, W_c is the calculated yield, W_m is the measured yield and $\sigma_m(i)$ is the uncertainty in the measured yield. Here

$$W_c(i) = 1 + Q_2 A_2 \left(\frac{5}{2} \right) P_2(\cos\theta) + Q_4 A_4 \left(\frac{5}{2} \right) P_4(\cos\theta), \tag{4.35}$$

where the $A_2(\frac{5}{2})$ and $A_2(\frac{5}{2})$ coefficients depends on δ. We varied $\arctan\delta$ from $-\pi/2$ to $\pi/2$ in 1000 steps, with each step size being approximately 0.0032. This assured a range for δ from $(-\infty, \infty)$. At each point the χ^2 value was recorded and plotted. As Fig. 4.17 shows, the minimum χ^2 value obtained using this method corresponded to $\delta = 0.02$. Its 68% confidence level uncertainty was determined from the range of δ values for which $\chi^2 = \chi^2_{\min} + 1$. This yielded a final result $\delta = 0.02(1)$.
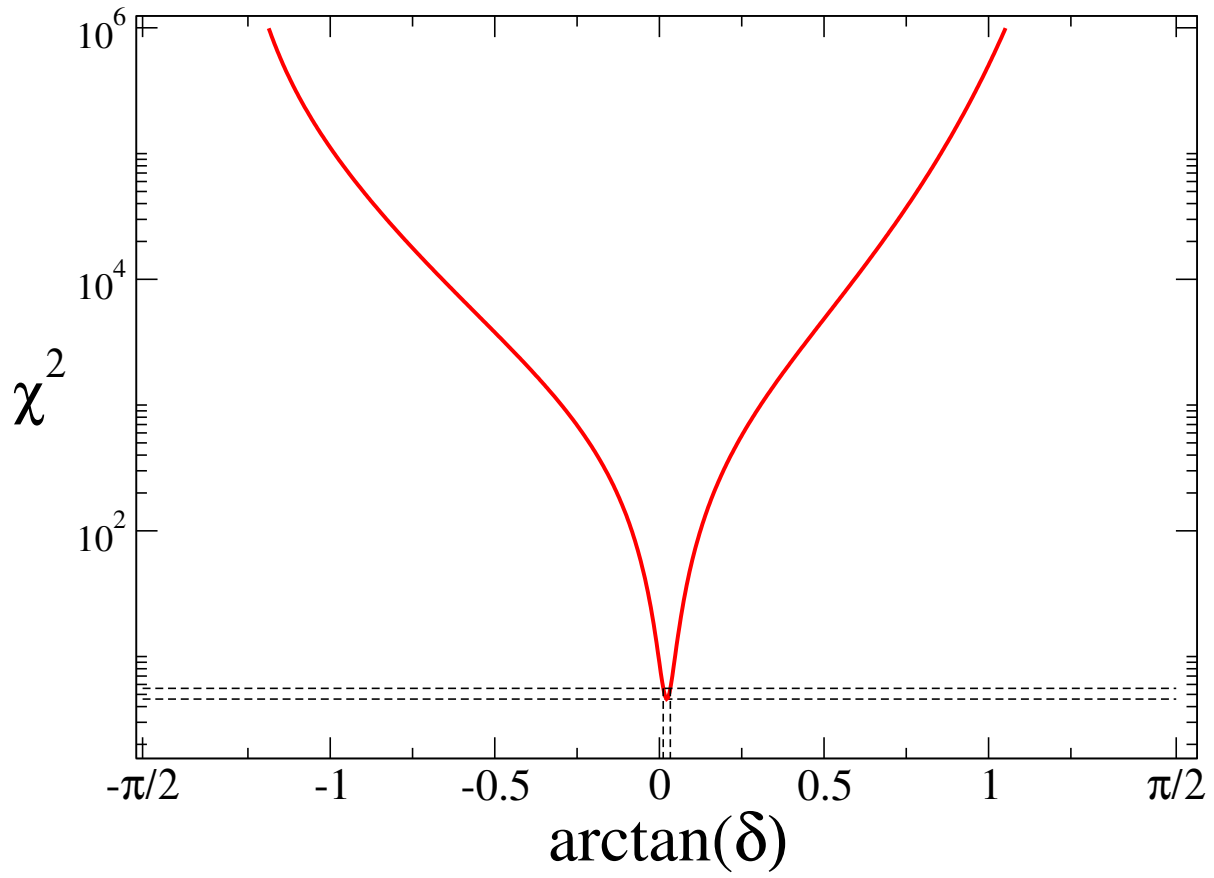
60

Figure 4.17: χ^2 as a function of $\arctan(\delta)$ from this measurement.

Chapter 5

Conclusions

This work shows that the mixing ratio of the $5/2_2^+ \to 3/2_1^+$, transition in ^{21}Na is more than 3 times smaller than previously determined. This implies that the transition is dominated by the $M1$ multipolarity. The consequence of this result in terms of the astrophysical implications is shown in Fig. 5.1. It compares the angular distribution based on the present mixing-ratio measurement, to the one assumed by Lyons *et al.* [1].

As described in Chapter 2, Section 2.5, Lyons *et al.* conducted measurements of the resonance strength and the yields of the 1113 keV resonance. The former was taken with a γ-ray detector at 55°, whereas the yield measurement was taken at 90° to the beam. As can be observed from Fig. 5.1, the difference between the two distributions is negligible at 55°. The yield is enhanced at 90°, but only by around 10%. This would result in a similar increase in the ^{20}Ne$(p, \gamma)^{21}$Na reaction rate extracted by Lyons *et al.*.

62
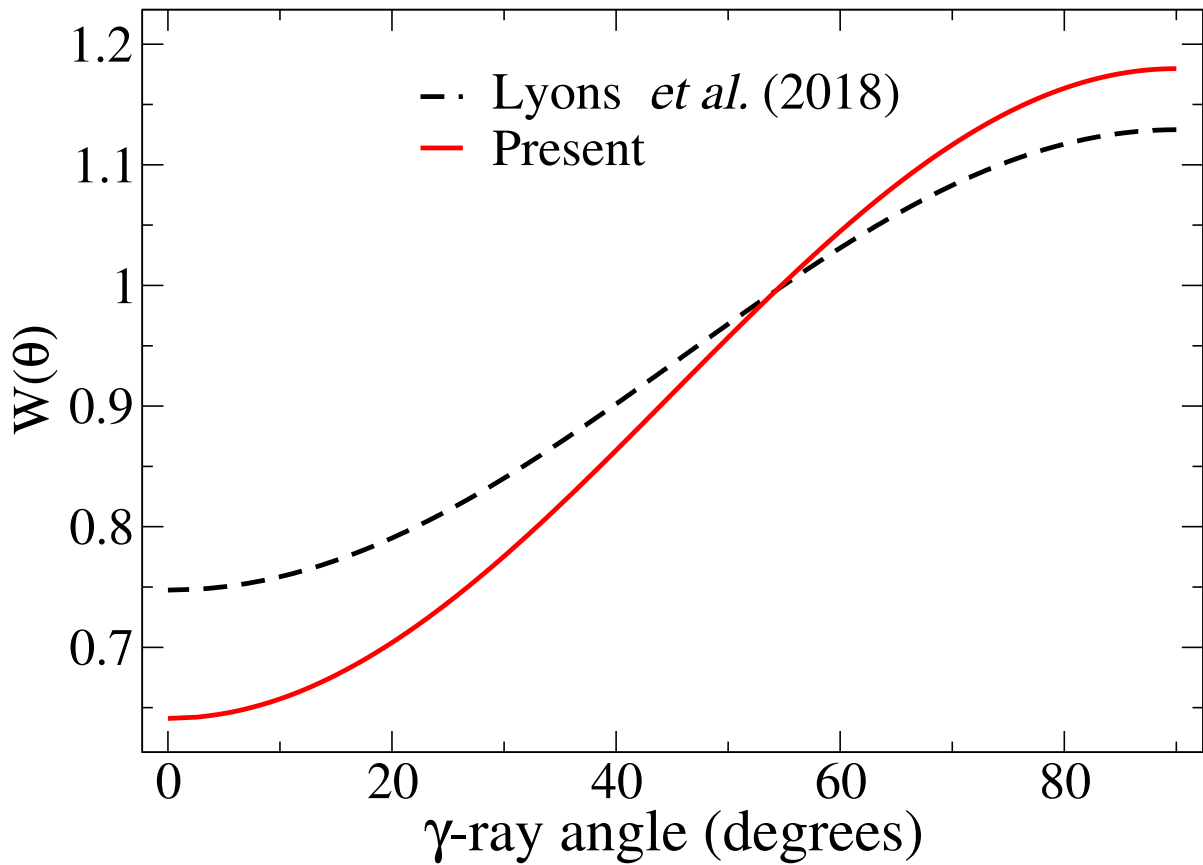
Figure 5.1: Comparison of the $W(\theta)$ used by Lyons *et al.* (Fig. 9, top-panel of Ref. [1]) to determine the ^{20}Ne(p, γ) astrophysical reaction rate and the angular distribution based on the mixing ratio determined from this work.

Bibliography

[1] S Lyons, J Görres, RJ deBoer, E Stech, Y Chen, G Gilardy, Q Liu, Alexander Makenzie Long, M Moran, D Robertson, et al. Determination of ^{20}Ne$(p, \gamma)^{21}$Na cross sections from E$_p$ = $500 - 2000$ keV. *Physical Review C*, 97(6):065802, 2018.

[2] Robert M Cavallo, Allen V Sweigart, and Roger A Bell. The production of sodium and aluminum in globular cluster red giant stars. *The Astrophysical Journal Letters*, 464(1):L79, 1996.

[3] Robert M Cavallo, Allen V Sweigart, and Roger A Bell. Proton-capture nucleosynthesis in globular cluster red giant stars. *The Astrophysical Journal*, 492(2):575, 1998.

[4] C Van der Leun and WL Mouton. The reaction ^{20}Ne(p, γ) ^{21}Na. *Physica*, 30(2):333–340, 1964.

[5] Claus E Rolfs, William S Rodney, and William S Rodney. Cauldrons in the cosmos: Nuclear astrophysics. *University of Chicago press*, 1988.

[6] Michael A Seeds and Dana Backman. Foundations of astronomy. *Cengage Learning*, 2011.

[7] Chushiro Hayashi, Rēun Hōshi, and Daiichiro Sugimoto. Evolution of the stars. *Progress of Theoretical Physics Supplement*, 22:1–183, 1962.

[8] Ibrahim Semiz and Salim Oğur. Dyson spheres around white dwarfs. *arXiv preprint arXiv:1503.04376*, 2015.

[9] EG Adelberger, A García, RG Hamish Robertson, KA Snover, AB Balantekin, K Heeger, MJ Ramsey-Musolf, D Bemmerer, A Junghans, CA Bertulani, JW Chen, H Costantini, P Prati, M Couder, E Uberseder, M Wiescher, R Cyburt, B Davids, S J Freedman, M Gai, D Gazit, L Gialanella, G Imbriani, U Greife, M Hass, WC Haxton, T Itahashi, K Kubodera, K Langanke, D Leitner, M Leitner, P Vetter, L Winslow, LE Marcucci, T Motobayashi, A Mukhamedzhanov, RE Tribble, Kenneth M Nollett, FM Nunes, TS Park, PD Parker, R Schiavilla, E C Simpson, C Spitaleri, F Strieder, HP Trautvetter,

K Suemmerer, and S Typel. Solar fusion cross sections. ii. the *pp* chain and cno cycles. *Rev. Mod. Phys.*, 83:195–245, Apr 2011.

[10] Christian Iliadis. Nuclear physics of stars. *John Wiley Sons*, 2015.

[11] Icko Iben Jr and Alexander V Tutukov. Supernovae of type i as end products of the evolution of binaries with components of moderate initial mass (m not greater than about 9 solar masses). *The Astrophysical Journal Supplement Series*, 54:335–372, 1984.

[12] AGW Cameron. Endpoints of stellar evolution. *Frontiers of Astrophysics*, pages 118–146, 1976.

[13] Axel Boeltzig, CG Bruno, Francesca Cavanna, Sergio Cristallo, T Davinson, R Depalo, RJ deBoer, A Di Leva, Federico Ferraro, Gianluca Imbriani, et al. Shell and explosive hydrogen burning. *The European Physical Journal A*, 52(4):1–13, 2016.

[14] Katharina Lodders. Solar system abundances of the elements. *Principles and Perspectives in Cosmochemistry*, 2, 10 2010.

[15] Jaroslav Merc, R Gális, and M Wolf. New online database of symbiotic variables: Symbiotics in x-rays. *Astronomische Nachrichten*, 340(7):598–606, 2019.

[16] James W Truran. Nuclear theory of novae. *Essays in Nuclear Astrophysics*, page 467, 1982.

[17] James W Truran. Nucleosynthesis. *Annual Review of Nuclear and Particle Science*, 34(1):53–97, 1984.

[18] B Paczynski, P Eggleton, S Mitton, and J Whelan. Structure and evolution of close binary systems. In *IAU Symp.*, volume 73, page 75, 1976.

[19] LI Antipova. Book-review-the symbiotic phenomenon. *Soviet Astronomy*, 34:329, 1990.

[20] JS Gallagher and S Starrfield. Theory and observations of classical novae. *Annual review of astronomy and astrophysics*, 16(1):171–214, 1978.

[21] Christian Iliadis, John M D'Auria, Sumner Starrfield, William J Thompson, and Michael Wiescher. Proton-induced thermonuclear reaction rates for a= 20–40 nuclei. *The Astrophysical Journal Supplement Series*, 134(1):151, 2001.

[22] C Rolfs, WS Rodney, MH Shapiro, and H Winkler. Hydrogen burning of ^{20}Ne and ^{22}Ne in stars. *Nuclear Physics A*, 241(3):460–486, 1975.

[23] Kenneth S Krane, David Halliday, et al. *Introductory nuclear physics*, volume 465. Wiley New York, 1988.

[24] Alejandro Garcia and Ernest M Henley. Subatomic Physics. *World Scientific Publishing Company*, 2007.

[25] George Gamow. The quantum theory of nuclear disintegration. *Nature*, 122(3082):805–806, 1928.

[26] Ronald Wilfrid Gurney and Edward Uhler Condon. Quantum mechanics and radioactive disintegration. *Physical Review*, 33(2):127, 1929.

[27] John Markus Blatt and Victor Frederick Weisskopf. Theoretical nuclear physics. *Courier Corporation*, 1991.

[28] Ian J Thompson and Filomena M Nunes. Nuclear reactions for astrophysics: principles, calculation and applications of low-energy reactions. *Cambridge University Press*, 2009.

[29] George Raymond Satchler. Introduction to nuclear reactions. *Macmillan International Higher Education*, 1990.

[30] Livius Trache. Indirect methods for nuclear astrophysics with radioactive nuclear beams. In AIP Conference Proceedings, volume 1213, pages 125–136. *American Institute of Physics*, 2010.

[31] J Sakurai and J Napolitano. Modern quantum mechanics 2nd edition. *Person New International edition*, 2014.

[32] Jun John Sakurai. Advanced quantum mechanics. *Pearson Education India*, 2006.

[33] John S Townsend. A modern approach to quantum mechanics. *University Science Books*, 2000.

[34] Samuel SM Wong. Introductory nuclear physics. *John Wiley & Sons*, 2008.

[35] ME Rose. The analysis of angular correlation and angular distribution data. *Physical Review*, 91(3):610, 1953.

[36] HJ Rose and DM Brink. Angular distributions of gamma rays in terms of phase-defined reduced matrix elements. *Reviews of Modern Physics*, 39(2):306, 1967.

[37] Richard D Gill. Gamma-ray angular correlations. *Academic Press*, 1975.

[38] RB Firestone. Nuclear data sheets for A = 21. *Nuclear Data Sheets*, 127:1–68, 2015.

[39] National Nuclear Data Center, Brookhaven National Laboratory, nudat (nuclear structure and decay data). (9 March 2022), March 18 2008.

[40] Erik C Mohrmann. Precise measurement of the $^7Be(p,\gamma)^8B$ S-factor. PhD thesis, *University of Washington*, 2008.

[41] Lutendo Phuthu. Analysis and simulations to obtain the weak magnetism term in ^{22}Na beta decay. PhD thesis, *University of the Western Cape*, 2016.

[42] S Triambak, A Garcia, D Melconian, M Mella, and O Biesel. Excitation energies in ^{32}S$(p,\gamma)^{33}$Cl, volume 74. *APS*, 2006.

[43] Philip R Bevington and D Keith Robinson. Data reduction and error analysis. *McGraw-Hill, New York*, 2003.

[44] Francesc Salvat, José M Fernández-Varea, Eduardo Acosta, and J Sempau. Penelope, a code system for monte carlo simulation of electron and photon transport. In *Proceedings of a Workshop/Training Course, OECD/NEA*, pages 5–7, 2001.

[45] Glen Cowan. Statistical data analysis. *Oxford University Press*, 1998.

[46] William H Press, Saul A Teukolsky, Brian P Flannery, and William T Vetterling. Numerical recipes in Fortran 77: volume 1, volume 1 of Fortran numerical recipes: the art of scientific computing. *Cambridge university press*, 1992.